Automatic estimation of daily volcanic sulfur dioxide gas flux from TROPOMI satellite observations: application to Etna and Piton de la Fournaise

Raphaël Grandin[1], Marie Boichu[2], Théo Mathurin[3], and Nicolas Pascal[3]

[1]Institut de Physique du Globe de Paris, Université Paris Cité, ForM@Ter

[2]Laboratoire d'Optique Atmosphérique, Université de Lille, CNRS

[3]AERIS/ICARE, Université de Lille, CNRS

Keywords (up to 6)

Satellite imagery / Sentinel-5P TROPOMI / Sulfur dioxide (SO_2)

Volcanic gas flux / Automated and interactive analysis

Real-time seismic amplitude (RSAM)

Index terms (1 to 5)

- 8430 Volcanic gases
- 8485 Remote sensing of volcanoes (4337)
- 0370 Volcanic effects (4301, 8409)
- 8419 Volcano monitoring (4302, 7280)
- 0520 Data analysis: algorithms and implementation

Key Points:

- Daily volcanic SO_2 flux is deduced from TROPOMI satellite imagery by mass-to-distance regression, including a noise estimation procedure
- SO_2 emission rates at Etna, during episodes of passive and eruptive degassing, demonstrate a good correlation with seismic energy
- The algorithm is made available to all as an open-source Python package and on the interactive web application "SO_2 Flux Calculator"

Corresponding author: Raphael Grandin, `grandin@ipgp.fr`

Abstract

Understanding the dynamics of sulfur dioxide (SO_2) degassing is of primary importance for tracking temporal variations in volcanic activity. Here we introduce the novel "disk method", which aims at estimating the daily volcanic SO_2 mass flux from satellite images (such as those provided by Sentinel-5P/TROPOMI). The method calculates a "proto-flux" using a regression, as a function of distance, of SO_2 mass integrated in a series of nested circular domains centered on a volcano. After regression, a single multiplication by plume speed suffices to deduce the SO_2 mass flux, without requiring a subsequent regression. This way, a range of plume speed and plume altitude scenarios can be easily explored. Noise level in the image is simultaneously evaluated by the regression, which allows for estimating posterior uncertainties on SO_2 flux and improving the level of detection for weak sources in noisy environments. A statistical test is also introduced to automatically detect occurrences of volcanic degassing, lowering the risk of false positives. Application to multi-year time-series at Etna (2021) and Piton de la Fournaise (2021–2023) demonstrates (a) a reliable quantification of SO_2 emissions across a broad range of degassing styles (from passive degassing to effusive or paroxysmal events), and (b) a reasonable day-to-day correlation between SO_2 flux and seismic energy. The method is distributed as an open-source software, and is implemented in an interactive web application within the "Volcano Space Observatory Portal", facilitating near-real-time exploitation of the TROPOMI archive for both volcano monitoring and assessment of volcanic atmospheric hazards.

Plain Language Summary

Volcanic eruptions emit sulfur dioxide gas (SO_2) into the atmosphere, which may cause harm to populations and the environment, and need to be monitored. Tracking volcanic emissions is also important for volcanologists to detect changes on a given volcano, and anticipate eruptions. SO_2 can be observed by satellites every day, but exploitation of satellite imagery requires complex procedures. Wind speed is a crucial ingredient, but it is often poorly known, leading to large uncertainties in estimated SO_2 mass. Here, a simple algorithm is proposed for analyzing SO_2 images provided by satellites. The mass of SO_2 is extracted in an area surrounding a volcano (typically 500 km) to estimate the quantity of SO_2 released, as well as associated uncertainties. Plume speed information can be incorporated after running the algorithm, which facilitates testing different plume speed scenarios. Application to Etna and Piton de la Fournaise volcanoes shows that temporal variations of SO_2 emissions follow the same pattern as seismic energy recorded by ground seismometers, which gives confidence in the results. The algorithm is made available to all as open-source code and in an open-access interactive web application within the framework of the "Volcano Space Observatory Portal".

1 Introduction

The release of volcanic material into the atmosphere, in the form of lava, tephra, aerosols and gas, represents a major source of hazard for populations living in the vicinity of volcanoes (Loughlin et al., 2015). Volcanic emissions can also put aircrafts at risk (Prata & Rose, 2015) and lead to a deterioration of air quality (Stewart et al., 2022). Among the various species of volcanic gases, sulfur dioxide (SO_2) is of primary importance, since it is the main precursor of sulfate aerosols, which can affect climate (e.g. Marshall et al., 2022, and references therein). Furthermore, since it separates from magma at shallow depth, SO_2 is the most effective gas species for tracking the dynamics of volcanic activity using remote sensing techniques, a task facilitated by its characteristic spectral signature and low background concentration in the atmosphere (Oppenheimer et al., 2011). Alongside measurements of ground deformation, estimating the SO_2 budget of a given volcano places constraints on the architecture of magma reservoirs, especially on the volume of magma stored or transported during periods of passive degassing, unrest, or during effusive or explosive eruptions (Girona et al., 2014; Kilbride et al., 2016; Shreve et al., 2022).

For any given eruption, the primary SO_2 emission parameters that need to be constrained are (i) the emission rate, or mass flux, and (ii) the altitude of emissions, or injection height. Emission rate is indicative of the dynamics of the eruption, and may change by orders of magnitude over time scales as short as a few hours, and is therefore a prime target for volcano monitoring (e.g. Aiuppa et al., 2015). On the other hand, constraining emission height is critical for Volcanic Ash Advisory Centers (VAAC), as it is essential for initializing simulations of atmospheric transport and accurately predicting the trajectory and lifetime of volcanic parcels (e.g. Stohl et al., 2011; Brenot et al., 2014; Boichu et al., 2015). In theory, plume injection height scales with the fourth root of the eruptive mass flux (Morton et al., 1956; Sparks et al., 1997). However, the relationship is in reality subject to substantial variability (e.g. see the compilations by Mastin et al., 2009; Aubry et al., 2023), due to the dependency of the dynamics of plume ascent upon external factors (e.g. atmospheric conditions, Tupper et al., 2009) or internal factors (e.g. particle grain-size distribution, Girault et al., 2014). Hence, deriving the emission rate directly from the plume height, or vice-versa, is not straightforward. When possible, the two quantities need to be constrained independently.

SO_2 emissions can be tracked from the ground using networks of UV-DOAS instruments installed near the volcanic source (e.g. Arellano et al., 2021), which are capable of measuring weakly- to moderately-degassing sources, such as events of transient pre-eruption degassing, or continuous, passive degassing. Unfortunately, a minority of active volcanoes are monitored from the ground, mainly due to a lack of resources (Loughlin et al., 2015). Furthermore, the viewing geometry from the ground means there is a limited view of the plume. Hence, when activity escalates, observation from ground sensors may become less reliable, or even fail entirely, especially near the source where a high abundance of ash and aerosols may lead to plume opacification (e.g. Andres & Schmid, 2001; Kern et al., 2012; Boichu et al., 2015; Kern et al., 2020). During large eruptions, personnel safety may also be threatened (e.g. at Merapi in 2010 or Soufrière Saint Vincent in 2021, see Surono et al., 2012; Joseph et al., 2022, respectively). As a consequence, satellite remote sensing is currently being considered as a cost-efficient way to complement ground-based observation systems and lessen the risk of observational gaps and biases (National Academies of Sciences, Engineering, and Medicine, 2017). In this context, it is essential to develop efficient, automatic and portable algorithms to leverage the wealth of satellite data currently available. This will better assist local observatories, decision-makers and the atmospheric and volcanology science communities in their respective tasks (Pritchard et al., 2022).

Today, SO_2 abundance in the atmosphere can be mapped by various imaging hyperspectral sensors onboard low-Earth orbit platforms (see Carn et al., 2016; Theys et al., 2019; Hyman & Pavolonis, 2020, and references therein), either operating in the ultraviolet (e.g. Sentinel-5 Precursor/TROPOspheric Monitoring Instrument, hereafter referred to as "TROPOMI", Aura/OMI, Suomi NPP/OMPS) or infrared domains (e.g. MetOp/IASI, JPSS/CrIS, Aqua/AIRS). These systems provide near-global coverage every 24 h for UV, or 12 h for IR (IR sensors being capable of both daytime and nighttime acquisitions), with a spatial resolution ranging from 5 km to 50 km, achieving variable levels of sensitivity with altitude (UV sensors being more sensitive to low-altitude SO_2). SO_2 detection can also be achieved at higher temporal resolution by geostationary sensors (every 10–15 minutes for MSG/SEVIRI, GOES/ABI or HIMAWARI/AHI, and exceptionally down to 30 seconds in on-demand zoom mode for GOES/ABI), or at higher spatial resolution by multispectral sensors in low-Earth orbit ($\sim$ 1 km pixel size for Aqua/MODIS, Suomi NPP/VIIRS, or 90 m for Terra/ASTER). However, these

specifications are obtained at the expense of the spectral resolution, which leads to a curtailment of the detection capability due to the presence of water vapor, ash or meteorological clouds (Thomas et al., 2011; Theys et al., 2019; Corradini et al., 2021).

Currently, TROPOMI provides the best spatial resolution among all hyperspectral sensors capable of daily near-global coverage (Theys et al., 2019; Fioletov et al., 2020), and will be the primary focus of this study.

To derive source terms (mass flux and altitude) from satellite images, it is necessary to account for the spatio-temporal evolution of gas parcels in the atmosphere, from their injection point to their observation location. Several approaches have been proposed to estimate volcanic flux from satellite images of SO_2 column amount (see also Theys et al., 2013, for a summary of the different methods):

1. the "Delta-M method" and "Box method" calculate the mass emitted in a known time interval (computed either from the mass burden in a single image, or by differencing between successive images), divided by the time span, correcting for an empirical gas loss rate (Krueger et al., 1996; Lopez et al., 2013; Theys et al., 2013; Coppola et al., 2019; Carboni et al., 2019).
2. "Plume traverses" consist of computing plume cross-sections (defined as the integral of column amounts on a transect perpendicular to the plume), followed by multiplication by plume speed (Carn et al., 2003; Merucci et al., 2011).
3. "Wind-rotation" methods apply a correction to compensate changing day-to-day plume directions and speeds, which makes it possible to fit a simplified model of gas transport, loss rate and dispersion, either on daily observations, or on stacked measurements providing monthly- or annually-averaged emission budgets released by "hotspots" (Beirle et al., 2014; Fioletov et al., 2016; Carn et al., 2017; Hyman et al., 2021; Fioletov et al., 2023).
4. "Inverse modelling" attempts to match the observed spatial distribution of vertical column densities against simulations from a numerical (chemistry-)transport model, initialized with a weather model, thereby incorporating potentially complex atmospheric processes such as diffusion, deposition and/or chemical conversion (Eckhardt et al., 2008; Kristiansen et al., 2010; Boichu et al., 2013; Theys et al., 2013; Flemming & Inness, 2013; Moxnes et al., 2014; Boichu et al., 2014, 2015; Vira et al., 2017; Heng et al., 2016; Cai et al., 2021; Behera et al., 2023).

5. the "Back-trajectory" approach estimates the time-of-flight of gas parcels associated with each pixel in a satellite image, and deduces time and altitude of emissions by back-projecting these individual parcels into the emission parameter space, using a back-trajectory model (Hughes et al., 2012; Queißer et al., 2019; Hayer et al., 2023; Markus et al., 2023; Esse et al., 2024).

Overall, these approaches all require knowledge of the plume direction (except for the simple "Delta-M method" of Krueger et al., 1996), plume speed, and often plume altitude. Unfortunately, these quantities can be uncertain, as they are derived from indirect information (e.g. meteorological reanalysis, radiosonde data, meteorological radar, or advanced satellite retrieval). Secondly, in order to mitigate the impact of background noise, these methods all apply a form of prior selection of points believed to be representative of volcanic emissions. This is achieved by outlining the plume boundary or by removing soundings with a low column amount, which introduces a bias whose impact is seldom quantified. Finally, none of the aforementioned methods is distributed as open-source code (except for the source separation algorithm of Markus et al., 2023) and none is associated with a publicly accessible web application.

Here, we introduce a novel method, hereafter designated as the "disk method", to estimate SO_2 flux released by a volcanic point source. The method starts with the computation of the SO_2 mass burdens integrated in a series of nested circular domains centered on a volcano (Figure 1a, Step 1). A regression is then performed to estimate the volcanic flux, which is predicted to behave as a linear term with distance, according to a "Gaussian plume" model, under the "slender plume approximation" (i.e. assuming that along-plume diffusion is negligible compared to advection speed). On the other hand, background noise is modeled as a "truncated normal distribution", acting as a quadratic term in the regression. The regression provides an estimation of the SO_2 flux and its associated uncertainty, together with a characterization of spatially-averaged noise in the input satellite data (Figure 1a, Step 2). The regression is wind-agnostic, rotation invariant, so that knowledge of plume speed or altitude can be accounted for at the post-inversion stage (Figure 1a, Step 3). Based on a statistical significance test, the method also allows for automatically detecting "true" SO_2 emissions sourced from the volcanic target and separating them from external perturbations.

In the next section, we present the gas and seismicity datasets analyzed in the paper. In Section 3 we describe the theoretical model and its algorithmic implementation. In Section 4 we assess the sensitivity of the inversion to free and internal parameters. In Section 5 we apply the method to a real dataset, computing long time-series with daily resolution on two volcanoes with contrasting dynamics (Etna, 2021 and Piton de la Fournaise, 2021–2023), examining the relationship between degassing and seismic energy. Finally, in Section 6 we provide recommendations on how to adjust the free-parameters of the method, and provide a few perspectives.

2 Data

2.1 SO_2 satellite imagery

TROPOMI provides daily near-global observations of trace gas and aerosols around 13:30 local solar time, with an approximate spatial resolution of 3.5×5.5 km at nadir (Veefkind et al., 2012). We use the TROPOMI Level-2 (L2) SO_2 product, with SO_2 retrieved at 1 km and 7 km altitude (Theys et al., 2022). The SO_2 retrieval in the L2 product is based on the DOAS technique (Theys et al., 2017).

For practical exploitation of TROPOMI data, an optional data preselection step may be applied. First, a preselection based on the column amount value may be performed, as retrievals may be considered as dominated by noise when the column amount is below a certain cutoff threshold (an operation hereafter referred to as "truncation"). The implications of truncation will be discussed specifically in the following sections. Furthermore, a certain number of swath-edge rows may be discarded, as SNR degrades close to the edge of the TROPOMI swath. For example, Fioletov et al. (2020) remove 20 swath-edge rows, but strictly following this criterion produces periodic observation gaps at low latitudes (within ±30°N). Hence, when applying the algorithm to real data in Section 5, only 7 columns will be removed to prevent gaps at Piton de la Fournaise (21.24°S), whereas 22 columns will be discarded at Etna (37.75°N). No further preselection is applied, in particular depending on sounding quality. Removal of dates based on spatially-averaged solar zenith angle or cloud fraction may be performed *a posteriori*, as discussed in Section 6.

All selected soundings acquired within a 24 hour time window are concatenated and resampled to a regular 0.05° × 0.05° grid (which corresponds roughly to a 5 km × 5 km

pixel size at the Equator). In the interior of the convex hull, we use a linear interpolation, with gap-filling up to a maximum distance of 1° from the closest valid pixel. No extrapolation is made outside the convex hull.

The resulting SO_2 column amount for each resampled pixel is noted p_i (expressed in Dobson Units or DU, where 1 DU = 2.69×10^{16} molecules.cm^{-2}). Each pixel is converted to an SO_2 columnar mass, noted x_i (expressed in kton) via a conversion formula $x_i = \kappa.p_i$, with $\kappa = 2.69\times10^{16}.\frac{M_{SO_2}}{N_{Avo}}.A$, where N_{Avo} is the Avogadro number, M_{SO_2} the molar mass of SO_2, and A the resampled pixel area. Hereafter, we use $A = 25$ km^2 (pixel size after regridding), such that $\kappa \approx 7\times10^{-4}$ kton.DU^{-1}.

Finally, SO_2 mass is integrated in circular regions centered on a volcano, by summation of the pixels located in the interior of a disk of radius r_n:

$$M(r_n) = y_n = \sum_{i=1}^{n} x_i \tag{1}$$

where i is the pixel index, x_i the pixel SO_2 mass, n the number of summed pixels, and $M(r_n)$ the integrated SO_2 mass. Thanks to the regridding step, the number of summed pixels in the summation domain, n, can be directly deduced from the radius r_n of the disk according to:

$$n = \frac{\pi r_n^2}{A} \tag{2}$$

2.2 Seismic data

Real-time seismic amplitude (RSAM, Endo & Murray, 1991) is often interpreted as a proxy for the lava discharge rate (e.g. Battaglia et al., 2005; Ichihara, 2016). In the absence of influences such as excess degassing or gas scrubbing, the mass of SO_2 emitted during an eruption is often considered proportional to the volume of erupted lava (e.g. Nadeau et al., 2011; Hibert et al., 2015). Hence, at first approximation, a direct comparison of RSAM and SO_2 flux can be used to assess the reliability of satellite-based estimations of SO_2 flux (e.g. Boichu et al., 2015; Hayer et al., 2023).

To compute the RSAM, raw seismic data is first converted to ground velocity by applying an instrument response correction. Data is then filtered between 1 Hz and 5 Hz, and RSAM is calculated over 60-seconds time windows. Comparison of RSAM with daily SO_2 time-series requires a specific procedure to correct for the time lag between the seismic measurement (which is synchronous with the emission of lava or gas) and the satellite

overpass (which measures the gas mass after its emission). We synchronize the seismic record to the temporal sampling of the satellite products by applying a causal rolling average filter to the RSAM time-series, with a window length θ (i.e. we replace each RSAM record at t by its mean in the preceding time interval $[t-\theta, t]$). Considering a characteristic length of the plume L_{plume}, and a plume speed u, we can deduce the appropriate delay using $\theta = L_{plume}/u$.

3 Methodology

3.1 Theoretical foundation for the "disk method"

3.1.1 Gaussian plume model

The advection-diffusion equation describes the distribution of mass concentration C for a gas during its transport and diffusion in the atmosphere. In Cartesian coordinates, and assuming an incompressible flow, this equation is expressed:

$$\frac{\partial C}{\partial t} + u_x\frac{\partial C}{\partial x} + u_y\frac{\partial C}{\partial y} + u_z\frac{\partial C}{\partial z} = D_x\frac{\partial^2 C}{\partial x^2} + D_y\frac{\partial^2 C}{\partial y^2} + D_z\frac{\partial^2 C}{\partial z^2} - kC + S \tag{3}$$

where emissions are described by the source term S, whereas gas loss is modeled by a sink term with first-order decay at constant rate k. The x, y, z components of advection velocity are u_x, u_y, u_z, the corresponding coefficients of diffusion are D_x, D_y, D_z, and time is noted t (Equation 18.11, p. 768 in Seinfeld & Pandis, 2016).

In order to simplify Equation 3, several assumptions are made:

- we assume steady-state ($\partial/\partial t = 0$), thus the source term S is constant.
- we consider a transport taking place in the x-direction (such that $u_y = u_z = 0$ and $u_x \neq 0$), which can be accommodated by a rotation of the coordinate system. Hereafter, we will note $u = u_x$.
- we use the "slender plume" approximation, which assumes that advection dominates over along-plume diffusion. This assumption corresponds to a large Péclet number P_e, i.e. $P_e = L\,u/D_x \gg 1$, with L a characteristic length. Taking the "e-folding distance" u/k as the characteristic length L (e.g. as in Hyman et al., 2021) translates the slender plume approximation into: $P_e = u^2/D_x\,k \gg 1$. The extent of the $P_e \gg 1$ domain, as a function of u, k and D_x is represented in Figure S1.

These simplifications allow for rewriting Equation 3 as:

$$u\frac{\partial C}{\partial x} = D_y\frac{\partial^2 C}{\partial y^2} + D_z\frac{\partial^2 C}{\partial z^2} - kC + S \tag{4}$$

The solution of this equation for a point source at $x = 0$, $y = 0$ and $z = 0$ releasing mass at a constant rate $\dot{m}$ (mass flux rate) can be written as:

$$C(x,y,z) = \frac{\dot{m}}{4\pi x\sqrt{D_y D_z}}.\exp\left\{\frac{-u}{4x}\left(\frac{y^2}{D_y} + \frac{z^2}{D_z}\right)\right\}.\exp\left\{\frac{-kx}{u}\right\} \tag{5}$$

where the classical Gaussian solution without gas loss (Equation 18.63, p. 777 in Seinfeld & Pandis, 2016) is multiplied by an exponential depletion factor (see e.g. Overcamp, 1982).

Satellite sensors provide SO_2 column amounts, which correspond to a mass per unit area integrated over a vertical column. In our plume model, vertical integration of concentration C in Equation 5 gives the following expression for the column amount D, which becomes independent of the vertical diffusion term:

$$D(x,y) = \int C(x,y,z)\,\mathrm{d}z = \frac{\dot{m}/u}{\sqrt{4\pi D_y(x/u)}}.\exp\left\{\frac{-uy^2}{4D_y x}\right\}.\exp\left\{\frac{-kx}{u}\right\} \tag{6}$$

Besides wind speed u, Equation 6 depends on two atmospheric parameters. First, the gas loss rate k, which can span many orders of magnitude, depending on plume properties and atmospheric conditions, in particular plume injection height (e.g. $k = 10^{-7} - 10^{-3}$ s^{-1}, according to Carn et al., 2016; Pattantyus et al., 2018). Hence, its reciprocal $\tau = 1/k$, the "e-folding time of gas loss", varies from tens of minutes to several days. In addition, in Equation 6, the horizontal cross-plume diffusion coefficient D_y (also known as the "cross-wind eddy diffusivity") describes the progressive cross-plume spreading of C with time, hence with distance from the source. Typical values for tropospheric volcanic plumes in the range of $D_y = 0.5 - 3 \times 10^4$ m^2.s^{-1} have been reported by Barr and Gifford (1987), whereas a lower $D_y = 0.1 \times 10^4$ m^2.s^{-1} was estimated for a 6 km-high plume at Etna by Tiesi et al. (2006). An example of a modeled column amount distribution is represented in Figure 2a, showing a Gaussian shape in any downwind cross-plume profile (yellow dots in Figure 2e). The validity of the plume model, in particular the slender plume approximation, as a function of D_y, k and u will be addressed in Section 4.

3.1.2 Relationship between integrated mass and mass flux

Integration of the column amount D of Equation 6 in a 2D circular domain of radius r centered on the volcano provides the total mass of SO_2, M_{volc}, released in the time interval $t \in [-T, 0]$, with $T = r/u$ (taking $t = 0$ for the acquisition time). To a first approximation, this circular integration is equivalent to integration over a semi-infinite rectangular domain perpendicular to the direction of transport, in the interval $x = [0, r]$:

$$M_{volc}(r) = \iint_{R=0}^{R=r} D(R)\mathrm{d}S \approx \int_{x=0}^{x=r} \int_{y=-\infty}^{y=+\infty} D(x,y)\,\mathrm{d}x\mathrm{d}y = \frac{\dot{m}}{k}\left(1 - \exp\left\{\frac{-kr}{u}\right\}\right) \quad (7)$$

Note that the equation remains valid if advection occurs in a direction different from the x-axis (rotation invariance). Furthermore, this expression becomes independent from cross-plume diffusivity D_y, and only depends on gas loss rate k.

A first-order expansion of Equation 7 yields a linear evolution of integrated mass as a function of distance r (yellow dots in Figure 2f):

$$M_{volc}(r) \approx \frac{\dot{m}}{u} r \quad (8)$$

The proportionality coefficient, $\left\{\frac{\dot{m}}{u}\right\}$, hereafter named "proto-flux", is a lumped quantity that condenses the advection speed u and proportional to the mass flux $\dot{m}$ averaged over the time interval $T = r/u$ before the image acquisition. The "proto-flux" can be estimated by linear regression of the integrated mass $M(r)$ *versus* distance r, where $M(r)$ is directly calculated from real data using Equation 1. In practice, the range of distances used in the regression needs to be optimized, depending on gas loss rate k.

The approximation of Equation 8 entails an underestimation of the "true" flux by a maximum 37% at $r = u/k$ (or, equivalently, at $T = \tau$). Thus, depending on the tolerance of the downstream application, Equation 8 may remain valid up to $r \approx u/k$. The effect of the maximum distance r_{max} used for fitting Equation 8 will be specifically discussed in Section 4, and recommendations for defining r_{max} will be provided in Section 6.1.

3.2 Pixel noise characterization

3.2.1 Spatially-averaged background noise

The value of an individual pixel in a TROPOMI image is the result of a retrieval algorithm, which translates raw radiance measurements into vertical column densities, or column amounts. In the following, we treat the mass x_i for pixel i as the realization of a

random variable X_i with expectation $E[X_i]$ and variance $Var(X_i)$. In what follows, we temporarily ignore the presence of volcanogenic or anthropogenic SO_2, to focus only on stochastic properties of the "background noise".

Any retrieval algorithm aims at optimizing the *accuracy* of the reported column amounts, which implies keeping $E[X_i]$ as close to zero as possible when the true gas concentration is zero. On the other hand, the pixel variance $Var(X_i)$ can be understood as the *precision* of the retrieval algorithm, and should be as small as possible.

The quality of the retrieval mainly depends on variations in surface reflectivity, solar zenith angle, atmospheric conditions, proximity to swath edge, 3D effects, while also depending on the retrieval algorithm itself (McCormick et al., 2013; Fioletov et al., 2020; Wagner et al., 2023). In the literature, the "uncertainty of the retrieval" is generally reported in the form of a single aggregated standard deviation "σ" (after appropriate unit conversion, $\sigma = \kappa.\sigma_{\mathrm{CA}}$, where pixel mass standard deviation σ is expressed in kton and pixel column amount standard deviation σ_{CA} is expressed in Dobson Units). For TROPOMI SO_2, a standard deviation $\sigma_{\mathrm{CA}} = 0.3$ DU is reported for the 7-km altitude product (Theys et al., 2019), and 1–1.5 DU for ground-level products (respectively, 1 DU over the tropics and 1.5 DU at high latitudes, Fioletov et al., 2020).

In practice, the actual value of the pixel standard deviation is variable in time and space. In the context of this study, we do not consider the spatial variability of noise, which is levelled out by the spatial integration of the SO_2 mass (Equation 1), such that the pixel index i can be dropped. Thus, σ_{CA} represents the level of noise averaged over a large number of pixels. On the other hand, temporal variations of the image quality are of primary importance, as they impact the uncertainty on the day-to-day integrated SO_2 mass (and thus SO_2 flux). Hereafter, the spatially-averaged standard deviation σ_{CA} is considered as an unknown that we estimate independently for each TROPOMI image.

3.2.2 Quadratic dependence of mass with distance in the presence of noise

In the presence of noise in an SO_2 satellite image, care should be taken in the spatial integration of pixel mass over a circular domain (Equation 7). Ignoring the influence of the volcanic plume, the summation formula for independent random variables gives an expression for the expectation of the random variable Y_n representing the integrated mass

M_n:

$$E[Y_n] = \sum_{i=1}^{n} E[X_i] = n.E[X] = \frac{\pi r_n^2}{A}.E[X] \tag{9}$$

where i is the pixel index and n is number of pixels in the summation (Equation 2). In Equation 9, since n is large, and following the same argument as for σ_{CA} in Section 3.2.1, pixel expectations $E[X_i]$ are replaced by a single spatially-averaged quantity $E[X]$.

Equation 9 indicates that the estimated volcanic flux will be *biased* by the presence of noise. Noise amplification will be proportional to both r_n^2 and $E[X]$, except in the ideal case where $E[X] = 0$.

3.2.3 Effect of truncation

In addition to intrinsic pixel noise, *truncation* represents a distinct, but potentially dominant contribution to a non-zero pixel expectation $E[X]$. Indeed, to mitigate the effect of noise when analyzing SO_2 satellite images, a common practice consists in masking pixels with low column amounts. For instance, Theys et al. (2019) recommend discarding pixels with values smaller than $3 \times \sigma_{\mathrm{CA}}$ for volcanic applications, in order to keep only values that are well above the noise. As a consequence of truncation of the lowest values, the mean pixel value will increase on average, henceforth biasing the expectation of the integrated pixel mass $E[Y_n]$ according to Equation 9.

For the sake of illustration, Figure 2 shows a synthetic TROPOMI image consisting of a superposition of (a) a plume and (b) random noise. The plume of Figure 2a is modeled using Equation 6, with parameters reported in the caption of Figure 2. Figure 2b represents noise only, assuming that individual pixel mass follows a zero-mean normal distribution. Figure 2c shows the result of summation of the plume and noise (Figure 2a + 2b), followed by truncation of pixels with column amounts below a cutoff threshold, hereafter noted CA_{min} (in Figure 2 we use $CA_{min} = 0.3$ DU). Ignoring the contribution of noise, integration of SO_2 mass in circular domains produces a nearly linear evolution with distance, as predicted from Equation 8 (yellow symbols in Figure 2f). However, addition of noise, combined with truncation, gives rise to a quadratic behaviour that progressively outweighs the contribution of the plume with distance from the source (green symbols in Figure 2f).

In what follows, we derive an expression for the curvature of the quadratic contribution of noise in presence of truncation (see Supporting Text S1 for full details). Following the

notations of Section 3.2.1, the pixel mass prior to truncation, noted X, is assumed normally-distributed, with expectation $E[X] = \kappa.\mu_{\text{CA}}$ and variance $Var(X) = \kappa^2.\sigma^2_{\text{CA}}$, where κ is the unit conversion factor defined above. Truncation corresponds to replacing pixel values x by a new value x', defined by: $x' = x$ if $x \geq \kappa.CA_{min}$, else $x' = 0$. The random variable describing pixel mass after truncation is noted X', and follows a *truncated normal distribution* (represented by the red part of the histogram in Figure 2b). Its expectation and variance, noted $E[X']$ and $Var(X')$, can be expressed analytically as a function of (i) the expectation $E[X]$ and variance $Var(X)$ of X prior to cutoff, and (ii) the truncation cutoff CA_{min} (e.g. Johnson et al., 1994, Chapter 13, Section 10.1). The expressions for $E[X']$ and $Var(X')$ are given in Supporting Text S1, Section S1.1, and the corresponding moments for integrated mass Y_n are provided in Section S1.2. In the particular case where $E[X] \approx 0$, the leading term in the expectation $E[Y_n]$ takes a simple Gaussian form, which allows for rewriting Equation 9 as:

$$E[Y_n] = \sqrt{\frac{\pi}{2}}.\frac{\kappa}{A}.\sigma_{\text{CA}}.\exp\left\{-\frac{1}{2}\left(\frac{CA_{min}}{\sigma_{\text{CA}}}\right)^2\right\}.r_n^2 \tag{10}$$

Equation 10 provides a closed-form expression for the quadratic bias, as a function of the pixel noise standard deviation σ_{CA} and truncation threshold CA_{min}. This expression is validated in an experiment with real TROPOMI data in Supporting Text S1, Section S1.3.

3.3 Flux estimation procedure

3.3.1 Forward problem formulation

Combining the plume model (Section 3.1, Equation 8: $M_{volc} \propto r_n$) and the noise model (Section 3.2, Equation 10: $M_{noise} \propto r_n^2$), the integrated mass in a disk of radius r_n centered on a volcano is expected to follow the regression model:

$$\begin{aligned} M(r_n) &= M_{volc}(r_n) + M_{noise}(r_n) + \epsilon_n \\ &= a.r_n + b.r_n^2 + \epsilon_n \end{aligned} \tag{11}$$

where we need to solve for a and b given $M(r_n)$ for a list of radii r_n. The linear term a represents the "proto-flux" $\left\{\frac{\dot{m}}{u}\right\}$ (Equation 8). The quadratic term b absorbs the bias inherited from the combination of pixel noise σ_{CA} and cutoff threshold CA_{min} (Equation 10). The cutoff CA_{min} may be adjusted on a case-by-case basis, and should be considered as a user-defined parameter, known *a priori*.

To complete the definition of the regression model, the error term ϵ_n should rigorously describe the uncertainties affecting observations $M(r_n)$, ideally in the form of a probability density function. Observations $M(r_n)$ are obtained by summation of the column amount for n pixels, where n is proportional to r_n^2 (Equation 2). The summed pixels have individual variances $Var(X_i)$, themselves proportional to σ_{CA}^2, and are assumed to be uncorrelated for simplicity. Hence, the variance formula for a linear combination of uncorrelated random variables implies that the variance of ϵ_n is proportional to both r_n^2 and σ_{CA}^2. Furthermore, n being large (typically > 1000), ϵ_n converges to a normal distribution. Since all biases are supposed to be already absorbed by the linear term $a.r_n$ (volcanic) and the quadratic term $b.r_n^2$ (noise), the residual (error) term ϵ_n can be considered zero-mean.

In summary, using the standard notation for a normal random variable:

$$\epsilon_n \sim \mathcal{N}\left(0, \gamma^2.\sigma_{\text{CA}}^2.r_n^2\right) \tag{12}$$

where the factor γ is an unknown proportionality factor that accommodates the linearity of aggregation of individual variances in the summation.

3.3.2 Inverse problem resolution

An inversion of the forward model of Equation 11 aims to provide estimates of the "proto-flux" $\hat{a}$ and noise strength $\hat{b}$, along with their associated posterior uncertainties, respectively $\hat{\sigma}_a$ and $\hat{\sigma}_b$ (where the "hat" symbol refers to estimated values). Full details of the inversion procedure are provided in Supporting Text S2. For brevity, only the key aspects are summarized below.

Importantly, Equation 12 entails that the standard deviation of observational uncertainties (error term ϵ_n) depends on r_n, hence is non-constant, which precludes using Ordinary Least-Squares. This issue can be tackled by weighting observations proportionally to the inverse of their standard deviation, ie. by $1/(\gamma.\sigma_{\text{CA}}.r_n)$ (e.g. see Sen & Srivastava, 2012, Chapter 6). As demonstrated in Supporting Text S2, Section S2.1, application of weights proportional to $1/r_n$ suffices to linearize the problem. As a result, a closed-form solution for $\hat{a}$ and $\hat{b}$ can be expressed using Weighted Least-Squares (Equation S15).

Estimating posterior uncertainties $\hat{\sigma}_a$ and $\hat{\sigma}_b$ requires a prior information on the pixel noise σ_{CA}. However, since pixel noise is variable in time and space, using a hard-coded (fixed) prior value for σ_{CA} will yield poorly representative results for the posterior uncertainties $\hat{\sigma}_a$ and $\hat{\sigma}_b$. Fortunately, as described in Supporting Text S2, Section S2.2, we can estimate the "true" spatially-averaged pixel noise $\hat{\sigma}_{\mathrm{CA}}$ directly from the quadratic term of the regression $\hat{b}$, by reversing Equation 10. The estimated pixel noise standard-deviation is expressed as:

$$\hat{\sigma}_{\mathrm{CA}} = \frac{CA_{min}}{\sqrt{W_0\left[\left(\sqrt{\frac{\pi}{2}}.\frac{\kappa}{A}.\frac{CA_{min}}{\hat{b}}\right)^2\right]}} \tag{13}$$

where W_0 is the first branch of the real-valued Lambert function (Equation S18). This expression is evaluated after the inversion, and the resulting pixel noise $\hat{\sigma}_{\mathrm{CA}}$ is used for estimating realistic posterior uncertainties $\hat{\sigma}_a$ and $\hat{\sigma}_b$ (Equation S16).

Here, instead of the simple linear solution described above, we use a more robust inversion procedure by further imposing prior bounds on a and b (which turns the problem into a non-linear one), and by including an additional constant term c in Equation 11 (intercept). Full details of the resolution of this generalized inverse problem are provided in Supporting Text S2, Section S2.3, and the numerical stability of the inversion procedure is demonstrated in Supporting Text S3.

3.3.3 Plume speed normalization

After inversion and estimation of posterior uncertainties, the final estimation of the mass flux $\hat{\dot{m}}$ (and its uncertainty $\hat{\sigma}_{\dot{m}}$) is deduced from the "proto-flux" $\hat{a}$ (and its uncertainty $\hat{\sigma}_a$) using Equation 8, i.e. by a simple multiplication by plume speed u:

$$\begin{bmatrix} \hat{\dot{m}} \\ \hat{\sigma}_{\dot{m}} \end{bmatrix} = u. \begin{bmatrix} \hat{a} \\ \hat{\sigma}_a \end{bmatrix} \tag{14}$$

This step is performed after the inversion, which makes it possible to adjust the plume speed, without necessitating a second inversion. A custom plume speed can be chosen, or, optionally in our implementation, the ECMWF ERA-5 wind fields can be queried (Hersbach et al., 2020; Copernicus Climate Change Service Climate Data Store (CDS), 2023) to deduce the appropriate plume speed based on a choice of plume altitude.

3.3.4 Statistical test for automatic detection of volcanic degassing

The inversion provides an estimate of the posterior uncertainty $\hat{\sigma}_a$ on retrieved "proto-flux" $\hat{a}$, which allows for testing the statistical significance of a detection of volcanic degassing. The null hypothesis is stated as $H_0 : \hat{a} = 0$ (i.e. *volcanic flux is insignificantly different from zero*), whereas the alternative hypothesis is $H_1 : \hat{a} > 0$ (i.e. *volcanic flux is significantly greater than zero*). For a given confidence level (or probability p), testing the null hypothesis corresponds to evaluating the inequality:

$$\frac{\hat{a}}{\hat{\sigma}_a} > F^{-1}(p) \tag{15}$$

where F^{-1} is the inverse of the cumulative density function of the standard normal (Gaussian) distribution, and $p \in [0.5 - 1.0]$ is the probability. If the inequality is satisfied, the null hypothesis is rejected, i.e. degassing is considered significant at the prescribed confidence level. As shown in Section 5.2, this statistical test allows for counterbalancing a temporary elevation of the noise level, for instance due to overpass by an external volcanic plume or anthropogenic SO_2-rich pollution, without raising a false positive.

3.4 Summary: inputs, outputs and internal parameters of the "disk method"

The "disk method" aims to estimate the volcanic SO_2 flux from the spatial distribution of SO_2 column amounts in a single TROPOMI image. The outputs of the method are (i) the SO_2 flux $\hat{\dot{m}}$, (ii) its uncertainty $\hat{\sigma}_{\dot{m}}$, and (iii) the characterization of noise in the image, in the form of a spatially-averaged pixel standard-deviation, $\hat{\sigma}_{\mathrm{CA}}$.

The first step consists in calculating the mass of SO_2 integrated in a series of circular domains centered on a volcanic target (Equation 1). From this input dataset, a second-order polynomial regression is applied to the vector of masses (one mass per disk radius), as a function of disk radius (Equation 11).

Based upon a Gaussian plume model (Equation 6), the linear term of the regression is shown to represent a "proto-flux", defined as a lumped quantity proportional to mass flux $\dot{m}$ (Equation 8). This plume model depends on three atmospheric parameters (the wind speed u, the cross-wind diffusivity D_y and the gas loss rate k) which are not retrieved by the inversion (unlike, e.g. Hyman et al., 2021). Indeed, the outputs are independent of the actual values of k, D_y and u, so long as they remain within certain ranges of validity (see Section 4).

The quadratic term absorbs the contribution of noise in the image (Equation 10). Injecting noise into the regression corresponds to taking an opposite approach to previous methods aiming at reconstructing daily SO_2 emission rates, which all apply a relatively conservative truncation to the data prior to processing (typically, three times the standard deviation on background column amount noise, e.g. Theys et al., 2019). Instead, we purposely apply a permissive (low) truncation threshold CA_{min}, which allows for lowering the overall level of detection on SO_2 flux. Furthermore, exploiting a bijective relationship with the noise standard deviation $\hat{\sigma}_{\mathrm{CA}}$ (Equation 13), this quadratic term is translated into a posterior uncertainty on the estimated SO_2 flux. This uncertainty (along with the estimated "proto-flux") make it possible to devise a simple statistical test for automatically flagging positive detections of an SO_2 emission from the volcanic target (Equation 15). The maximum distance of integration r_{max} and the threshold CA_{min} are the two free input parameters of the method. Their effect on the regression is described in Section 4, and recommendations for setting them are provided in Section 6.

Finally, the determination of the mass flux requires multiplying the "proto-flux" by an estimate of the plume speed u (Equation 14). This last step is carried out a posteriori, which facilitates exploration of a range of wind speed scenarios.

4 Sensitivity analysis and detection threshold

4.1 Theoretical detection threshold without gas loss and noise

The regression model in Equation 11 ignores the effect of truncation on the apparent linear term ($\hat{a}$). Yet, since pixels with a low column amount are masked prior to integration, truncation inevitably leads to an underestimation of the integrated mass $M(r_n)$, and with that, the retrieved SO_2 flux is expected to be affected too. As demonstrated in Supporting Text S4, in the simplifying case where k=0 (no gas loss) and σ_{CA}=0 (no noise), as long as the integration is limited to a maximum distance r_{max}, it is possible to derive a closed-form expression for the fraction of mass flux that is underestimated by the inversion as a result of truncation (here, a fixed fraction of 25% is chosen). This expression can be reformulated to define a lower bound for the detectable SO_2 mass flux:

$$\dot{m}_{min} = \frac{\kappa.CA_{min}}{A}\sqrt{4\pi D_y\, r_{max}\, u} \tag{16}$$

Figure 3a displays the detection threshold $\dot{m}_{min}$ (x-axis) depending on the maximum distance r_{max} (y-axis), for a scenario with $u = 10$ m.s^{-1} and $D_y = 10^4$ m^2.s^{-1}, and for a range of cutoff values CA_{min}. A higher cutoff threshold CA_{min} limits the possibility to detect low SO_2 fluxes, as gas concentration in the plume rapidly falls below the detection level beyond a certain distance r_{max}. For practical purposes, Figure 3a can be used as a reference chart to jointly adjust r_{max} and CA_{min} to a targeted detection threshold $\dot{m}_{min}$, given a certain wind speed u and reasonable bounds on D_y.

4.2 Valid ranges of gas loss rate (k) and diffusivity (D_y)

Next, we conduct an experiment to assess the sensitivity of the method to other internal parameters of the forward model, starting with the diffusivity D_y and gas loss rate k. We define a series of scenarios with variable levels of cutoff CA_{min}, ranging from 0.1 DU to 1.2 DU (Figure 3b). For each scenario, considering a fixed mass flux ($\dot{m} = 1$ kton.day^{-1}) and a fixed wind speed ($u = 10$ m.s^{-1}), we compute 2,000 simulated TROPOMI images, constructed from the superposition of a synthetic plume with random diffusivity D_y and random gas loss rate k (using Equation 6) and a synthetic noise with $\sigma_{\mathrm{CA}} = 0.3$ DU (corresponding to a "moderate noise" case). After application of the threshold CA_{min}, we compute the spatial integration of these synthetic TROPOMI images for a series of circular domains, up to $r_{max} = 500$ km. Finally, the synthetic data vector of integrated masses is fed into the inversion, and we compute the ratio R between the reconstructed mass flux $\hat{\dot{m}}$ and the "true" SO_2 mass flux $\dot{m}_{true}$ (i.e. $R = \hat{\dot{m}}/\dot{m}_{true}$). An exact reconstruction corresponds to $R = 1$, whereas $R = 0$ means a complete loss of sensitivity.

Figure 3b shows the domain of sensitivity of the inversion (defined as $R > 0.75$, i.e. a reconstructed mass flux no smaller than 75% of the "true" mass flux) as a function of k (y-axis) and D_y (x-axis). We observe that sensitivity is confined to a domain in the lower left quadrant of the graph, bounded by a maximum gas loss k_{max} and a maximum diffusivity $D_{y,max}$ (respectively, upper and right limits of the lower left quadrant in Figure 3b). When k or D_y exceed these critical values, the reconstructed SO_2 flux substantially underestimates the "true" value (hatched area in Figure 3b). As expected from Section 4.1, the sensitivity improves when CA_{min} is decreased.

We verify that the domain of sensitivity remains in the interior of the high Péclet number domain (i.e. $u^2 \gg D_x\, k$, assuming that $D_x \approx D_y$ for simplicity, double hatched area in the upper right corner of Figure 3b), consistent with the "slender plume approximation".

In terms of maximum gas loss, the inversion performs well up to a maximum $k_{max} \approx 2\text{–}5\times10^{-5}$ s^{-1}, equivalent to an e-folding time of $\tau = 6\text{–}14$ hours (Figure 3b). This bound materializes the limit of validity of the linear approximation of Equation 8: a high gas loss leads to an underestimation of the SO_2 flux by the inversion. The limit appears to be well approximated by the inverse of the characteristic time T defined in Section 3.1.2 (i.e. $k = 1/T = u/r$, setting r to the maximum radius $r_{max} = 500$ km used in the synthetic tests). Two factors likely contribute to stabilizing the linear term near $r \sim u/k$: (i) weighting by $1/r_n$ (Section 3.3.2), which counterbalances the influence of data points at large r, which are most affected by the exponential gas loss, and (ii) the beneficial side effect introduced by the quadratic term, which probably absorbs a fraction of the bias generated by the exponential decay. Thereafter, the criterion $r_{max} \lesssim u/k_{max}$ will be retained to define the maximum distance that may be used for the input dataset in the inversion (horizontal dotted lines in Figure S2).

The maximum diffusivity $D_{y,max}$ is consistent with the value obtained for D_y from Equation 16, replacing u, r_{max}, $\dot{m}$ and CA_{min} by the values used in the synthetic tests (vertical dashed lines in Figure S2). This observation confirms that the theoretical bound defined in Equation 16 can be effectively used to predict the maximum diffusivity allowed by the "disk method".

4.3 Influence of pixel noise (σ_{CA}) and wind speed (u)

Using the same approach as in Section 4.2, we now assess the sensitivity of the method in three cases considered representative of three noise scenarios (Figure 3c). Each scenario is empirically defined by a single pair of values for pixel noise σ_{CA} and cutoff threshold CA_{min}: (i) "low noise scenario": $(\sigma_{\mathrm{CA}}, CA_{min}) = (0.1, 0.2)$ DU; (ii) "moderate noise scenario": $(\sigma_{\mathrm{CA}}, CA_{min}) = (0.3, 0.9)$ DU; (iii) "high noise scenario": $(\sigma_{\mathrm{CA}}, CA_{min}) = (1.0, 3.0)$ DU. Contrary to the previous exploration where mass flux was held fixed and diffusivity was variable, here, we compute synthetic plumes with random mass fluxes $\dot{m}$ and a fixed diffusivity $D_y = 10^4$ m^2.s^{-1} (a value representative of tropospheric plumes, see Section 3.1). The gas loss rate k remains random.

In Figure 3c, the domain of stability is displayed as a function of the mass flux $\dot{m}$ (x-axis) and gas loss rate k (y-axis). The boundary of the sensitivity domain for $\dot{m}$ (left limit of the lower right quadrant) allows for defining a detection threshold, or minimum detectable SO_2 mass flux. The exploration shows that the detection threshold increases from ≈ 0.5 to ≈ 5 kton.day^{-1} from low to high noise scenario.

Decreasing the distance of integration r_{max} improves the sensitivity (upper limit of the sensitivity domain). However, reducing r_{max} has a negative side effect on the ability of the inversion to correctly estimate the intensity of noise (not shown in Figure 3c, see Supporting Figure S5). We also note that decreasing the integration distance r_{max} improves the detection level for high gas loss scenarios (k). Nevertheless, the improvement is marginal, and in fact, wind speed u has a dominant effect.

In Figure 3d, we explore the primary effect exerted by wind speed u, holding all other parameters fixed according to the "low noise / short distance" scenario defined in the previous exploration (i.e. $(\sigma_{\mathrm{CA}}, CA_{min}) = (0.1, 0.2)$ DU and $r_{max} = 250$ km). We observe that a low wind speed improves the detection threshold due to an overall increase of gas concentration, as gas accumulates near the source, enhancing the sensitivity to weak fluxes (left limit of sensitivity domain bounded by the dashed yellow curve in Figure 3d). Nevertheless, a low wind speed also generates an adverse effect: as plume age increases at any given distance, a higher proportion of gas is degraded and lost in the area of integration. This leads to an underestimation of the SO_2 flux (upper limit of sensitivity domain in Figure 3d). Conversely, the effects are reversed for a high wind speed (dashed blue curve in Figure 3d): detection capability is slightly weakened (gas concentration is everywhere lower), but the inversion is much more tolerant to a high gas loss rate (gas parcels are "younger" at any distance). In summary, a low wind speed leads to a substantial underestimation of the SO_2 flux when gas loss rate is high.

5 Results: application to volcanic case-studies

5.1 Etna (January – December 2021)

5.1.1 Volcanic context

In order to investigate the capacity of the method to retrieve SO_2 emissions over long time-intervals, we analyze TROPOMI SO_2 data acquired at Etna volcano (elevation: 3,350 m asl) over a one-year-long period (1 Jan 2021 – 31 Dec 2021). Etna's volcanic

activity is characterized by a broad spectrum of eruption types and degassing activity, alternating between passive outgassing, effusive eruptions, and occasional Strombolian explosions (Giuffrida et al., 2023).

Etna is equipped with permanent ground monitoring networks of UV-DOAS instruments installed on the flanks of the volcano (FLAME network, Salerno et al., 2009), and with short-range UV cameras near the summit (Delle Donne et al., 2019). However, these data may be affected by temporal gaps and uncertainty due to changing atmospheric conditions, or the presence of ash (Boichu et al., 2015). The annually-averaged daily SO_2 mass flux has been estimated from satellite data to 2–3 kton.day^{-1} during passive degassing phases (Carn et al., 2016, 2017; Coppola et al., 2019; Fioletov et al., 2023), increasing to $\sim$ 4 kton.day^{-1} during effusive phases (Coppola et al., 2019; Queißer et al., 2019), with individual paroxysmal events typically releasing 5–20 kton SO_2 over time intervals of 3–12 hours (Boichu et al., 2015; Corradini et al., 2020; Sellitto et al., 2023).

Etna's activity has been particularly intense in 2021, fueled by two episodes of mafic recharge in late 2020 and mid-2021 (Giuffrida et al., 2023). A sequence of 62 intense explosions originating from the South East Crater, associated with lava fountains lasting from a few hours to a couple of days, are concentrated in two paroxysmal sequences (Aiuppa et al., 2015), which are mostly covered by our dataset: (a) between 13 December 2020 and 2 April 2021 and (b) between 19 May and 23 October 2021 (Figure 4).

5.1.2 Daily SO_2 flux for the year 2021

In a first analysis, the TROPOMI 7 km altitude product is used, removing 22 rows to reduce the impact of noise from track edges. The cutoff threshold is set to $CA_{min} = 0.0$ DU, and the maximum distance of integration to $r_{max} = 1000$ km. Cumulative masses are calculated for radii 25, 50, 75, 100, 150, 200, 250, 300, 400, 500 and 1000 km, and provided as input data for the inversion. We discard acquisitions with a mean cloud fraction $> 75\%$ within 200 km of the volcano (removing 35 dates out of 365). After inversion, plume speed is assumed equal to wind speed from the ERA-5 ECMWF product at a pressure level of 600 hPa (equivalent to an altitude of ≈ 4.2 km), which provides the best coherence between observed plume direction in the image and predicted wind direction over this one-year-long interval (Figure S6a).

Figure 4a shows the SO_2 daily flux estimated by the "disk method" for a 1-year-long time interval spanning the year 2021. Estimated SO_2 emission rates are highly variable in time, with isolated bursts exceeding 10 kton.day^{-1}, mainly clustered in February-March, May–July and October 2021 (Figure 4a). The largest SO_2 peaks reach $\sim$ 20 kton.day^{-1}, which is comparable in magnitude with (yet larger than) values estimated from ground observations (10–15 kton.day^{-1}, according to Aiuppa et al., 2023). These periods of intense degassing alternate with weeks-long intervals of lower emission rates, below 1 kton.day^{-1}, especially in April, October and November 2021. The "background" emission rate in these relatively quiet time intervals is estimated to 0.3–0.8 kton.day^{-1} from TROPOMI, commensurate with the 1 kton.day^{-1} reported by Aiuppa et al. (2023).

By integrating daily flux estimates over the full length of the 2021 time-series, we estimate a cumulative SO_2 mass of 443 kton for the year 2021 using the 7 km product. An alternative estimate obtained by performing a linear interpolation at 4.5 km (assumed plume height) between fluxes computed using the 1 km and 7 km products (analyzed independently with identical settings, both with CA_{min}=0.0 DU) yields a total mass of 915 kton (Figure S7). These values are reasonably consistent with the total annual emission budget of 600 kton for the same year, as reported by Fioletov et al. (2023, 2022) using an independent method for analysing TROPOMI data (keeping in mind that Fioletov et al. (2023, 2022) excluded days with large SO_2 mass burdens). We note that both the pixel noise and the flux estimated over Etna for 2021 from the TROPOMI 1 km product are 2–4 times larger than that from the 7 km product (Figure S7).

5.1.3 Comparison of degassing with RSAM

Further comparison with a ground-based dataset acquired at higher temporal resolution, such as seismicity, provides insights on the ability of satellite-based observations to capture temporal variations of volcanic activity. In Figure 4, the 1-year-long time-series of estimated SO_2 flux is compared to the seismic energy (RSAM) recorded continuously at seismic station ESLN, situated 4 km south of Etna's summit (Figure 4b). The temporal shift that needs to be applied to the RSAM data (Section 2.2) is estimated to $\sim$ 8 hours, considering a typical length of the plume of $\sim$ 500 km and a mean wind speed of $\sim$ 15 m.s^{-1} at 4 km asl.

Bursts of large gas emissions (flux > 7 kton.day^{-1}) all coincide with peaks of seismic energy (Figure 4b). On the other hand, periods of reduced degassing (April–May, October and December 2021) consistently match with seismically quiescent time intervals. Figure 4c shows a zoom spanning the May–August 2021 paroxysmal sequence, where volcanic activity at Etna was characterized by the occurrence of > 20 lava fountain events, lasting between 2 hours and > 24 hours, with a recurrence interval ranging from a few days to less than 24 hours on 21–27 June 2021 (INGV, 2021b). The day-to-day pattern of seismic energy release variations during this period is closely reproduced in the TROPOMI-derived SO_2 flux history (Figure 4c).

Quantitative comparison of the SO_2 emissions and seismic energy (RSAM) demonstrates a reasonable correlation between the two observables. A power-law fit indicates that the ground velocity is proportional to $\dot{m}^{\beta}$, with $\beta = 0.7 - 1.3$ (depending on the points selected, see Figure 4d). This relation is consistent with the near-proportionality between seismic energy and magma discharge rate reported in previous studies (e.g. see Ichihara, 2016, and references therein). Nevertheless, rapid intra-day fluctuations of volcanic activity can be aliased or even missed by our analysis, since we estimate a flux averaged over the time interval between gas emission and satellite acquisition. In addition, our assumption of a steady flux and constant emission height (here, 4.2 km asl) may be overly simplistic for the description of energetic events. For example, on 19 February 2021, the eruption lasted less than 3 hours, and the plume rose up to 10 km (INGV, 2021a; Global Volcanism Program, 2021). Detailed estimates of SO_2 flux for such short-lived events would require a case-by-case analysis.

5.2 Piton de la Fournaise (September 2021 – September 2023)

5.2.1 Volcanic context

In order to assess the capability of the method to constrain smaller emission rates, we now turn to Piton de la Fournaise (elevation: 2,600 m asl), one of the most active volcanoes in the world, producing an average of 2–3 eruptions per year for the past 30 years (Roult et al., 2012; Dumont et al., 2022). Eruptions are generally preceded by a months- to days-long period of pre-eruptive seismicity and inflation sourced from a reservoir ~ 2 km below the summit (Peltier et al., 2009). Vertical migration of seismicity and deformation over time scales of days to hours mark the ascent of magma toward the

surface (Roult et al., 2012; Smittarello et al., 2019). In the few hundred meters below the summit, the direction of magma migration often shifts, either toward the southern or northern rift zones, eventually feeding an effusive eruption that may last from a few hours to several weeks (Dumont et al., 2022; Journeau et al., 2023). More rarely, explosive eruptions, caldera collapse and lateral flank motion can be triggered. At the time of writing, the last such event occurred in 2007 (Michon et al., 2013).

Contrary to Etna, the SO_2 budget of Piton de a Fournaise is modest. SO_2 emissions are monitored by a network of three ground-based UV-DOAS instruments (NOVAC network). However, these measurements often substantially underestimate the SO_2 budget of the volcano, due to unfavorable atmospheric and geometric conditions (Arellano et al., 2021; Verdurme et al., 2022). Satellite observations of syn-eruptive SO_2 emissions of Piton de la Fournaise have also been analyzed (e.g. Khokhar et al., 2005; Carn et al., 2016; Verdurme et al., 2022). A SO_2 mass of 230 kton was released during the reservoir collapse of 2007 (Tulet & Villeneuve, 2011), but smaller eruptions generally release 10–35 kton of SO_2 (Carn et al., 2016; Verdurme et al., 2022; Hayer et al., 2023), consistent with the release of $<$ 20–30 Mm^3 of bulk lava reported from field and satellite observations (Roult et al., 2012; Verdurme et al., 2022). To date, no inter-eruptive satellite detection of SO_2 has been reported.

5.2.2 Comparison of SO_2 flux and RSAM for three eruptions

Here, we analyze the three latest eruptions of Piton de la Fournaise (at the time of writing): December 2021 – January 2022 (Figure 5a), September – October 2022 (Figure 5b) and July – August 2023 (Figure 5c). The three eruptions have similar duration (several weeks), style (effusive) and volume of extruded lava ($\sim$ 10 Mm^3).

To retrieve SO_2 fluxes from TROPOMI, we use the 7 km altitude product, integrated up to a maximum distance of 500 km, as the plume rarely extends beyond this distance. To prevent gaps due to increased spacing between TROPOMI tracks at low latitude, we only mask 7 swath-edge rows. As a result, the SO_2 column amount maps include more noise from swath-edge rows than at Etna, and the progressive longitudinal drift of the swath during Sentinel-5P's orbital cycle generates periodic modulations of the ambient noise. Finally, we assume that plume speed is equal to wind speed at the ERA-5 700 hPa

pressure level ($\approx$ 3 km). This altitude best matches with the plume transport direction visible in syn-eruptive TROPOMI images (Figure S6b).

Comparison between SO_2 and RSAM is displayed in Figure 5. For RSAM, we use data from three seismic stations selected for their short distance from the active vents of each eruption (respectively, FOR, RVA and PVD). We decrease the time lag for the seismic-to-satellite synchronization down to 5 hours, because volcanic plumes are typically shorter at Piton de la Fournaise than at Etna.

The September – October 2022 eruption (Figure 5b) is characterized by an initial pulse of SO_2 on 20 September reaching 3 kton.day^{-1}, followed by a week-long period of weaker emissions at 1 kton.day^{-1}. The last 5 days of the eruption are marked by an increase of degassing, reaching a maximum of 5 kton.day^{-1} on the last day of the eruption. This progressive increase in SO_2 flux coincides with a coeval rise in seismic energy, until both signals drop abruptly on 5 October 2022, when the eruption ceases. The same pattern is also apparent in time-averaged discharge rates reported independently by the MIROVA and HOTVOLC services using MODIS, VIIRS and MSG-SEVIRI data (see Figure S9, adapted from Chevrel et al., 2023). This eruption occurred during a period of exceptionally dry weather, with a cloud cover $< 25\%$ for most of the eruption (blue symbols in Figure 5b), October 2022 being the driest October since the first measurements at La Réunion in 1972 (Météo-France, 2022b). This favorable situation facilitates the agreement between RSAM and satellite-based estimations of emission rates.

The July – August 2023 eruption (Figure 5c), in spite of a longer duration (38 days), displays a similarly consistent evolution between degassing and seismicity. The eruption started on 2 July 2023 with a one-week-long phase of intense seismic energy release, followed by a temporary lull, and a resumption of activity on 8 July 2023. After that, a continuous exponential-like decay is observed until the eruption end one month later. During the decay phase, in spite of the low SO_2 fluxes involved (less than 0.6 kton.day^{-1}), the "disk method" consistently tracks the progressive decrease of SO_2 emission rate, and successfully detects surges coinciding with temporary increases in RSAM on 26–27 July and 8 August (last day of the eruption). Remarkably, during this decay phase, in spite of substantial day-to-day fluctuations of wind speed (between 1 m.s^{-1} and 10 m.s^{-1}, green symbols at the bottom of Figure 5c), the estimated SO_2 flux remains relatively stable. This suggests that the method correctly compensates for the dilution (respectively, the

accumulation) of SO_2 resulting from an increase (respectively, a decrease) of transport speed.

Remarkably, in addition to smooth fluctuations of activity, the two eruptions of September–October 2022 and July–August 2023 are both characterized by an initial large pulse of degassing at the onset of the eruption, greater than in the following days by a factor ~ 3. Simultaneously, a spike of seismic energy is detected. These observations may be interpreted as "uncorking" events, where a pressurized batch of gas is suddenly released when the dike connects to the surface.

In contrast with the two 2022 and 2023 eruptions, comparison between SO_2 emissions and RSAM during the December 2021 – January 2022 eruption (Figure 5a) is not straightforward. The RSAM displays a progressive increase of seismic energy over the full duration of the eruption, punctuated by quasi-periodic fluctuations in the first two weeks. These two features (progressive rise and fluctuations) are not visible in the SO_2 flux.

At least part of this apparent disagreement may be attributed to meteorological conditions affecting the quality of SO_2 measurements. A clear and systematic decrease in the apparent SO_2 flux is observed when the cloud fraction is high (blue symbols at the bottom of Figure 5a). In fact, windy and cloudy weather was reported during most of the December 2021 – January 2022 eruption, including an exceptionally intense rain episode on 22–23 December 2021, and stormy rains on 8–15 January 2022 (Météo-France, 2021, 2022a). On the other hand, during this eruption, variations in RSAM have probably been influenced by small-scale processes taking place around the vent, such as phases of cone construction and collapse, as well as channelling of lava into lava tunnels or cone overflow (as described in the eruption report of Observatoire volcanologique du Piton de la Fournaise, 2022). These surface processes modulate the relationship between the lava and gas discharge rate and the amplitude of seismic tremor (e.g. Battaglia et al., 2005; Journeau et al., 2023), hence complicating direct comparison. We acknowledge that both factors (cloud cover and small-scale processes at the vent) are not mutually exclusive. A systematic analysis of day-to-day observations would be necessary to quantify the influence of these different factors.

Eventually, by summing daily-averaged SO_2 fluxes over the duration of each eruption, the total SO_2 mass budget can be estimated. The three eruptions released 19.1 kton SO_2 (December 2021 – January 2022 eruption), 23.1 kton SO_2 (September – October 2022

eruption) and 17.7 kton SO_2 (July – August 2023 eruption), with a $\sim 15\%$ relative 1-σ formal uncertainty. These estimates are increased by a factor ~ 3 when the 1 km altitude product is used, instead of the 7 km product (Figure S8). Due to the cloudy conditions prevailing at that time, estimates for the December 2021 – January 2022 eruption likely represent an underestimation of the SO_2 budget, perhaps by a factor of two or more.

5.2.3 Automatic detection of degassing for a 2-year-long time-series

In order to assess the stability of the results and the capability of the statistical test of Equation 15 to provide reliable detections of volcanic degassing, we analyze a complete, two-year-long time series of TROPOMI data over Piton de la Fournaise (Figure 6). The period includes the three aforementioned eruptions, and is analyzed using the same parameters (7 km product; maximum distance 500 km; $CA_{min} = 0.0$ DU; masking 7 swath-edge rows). With a probability threshold fixed to $p = 99\%$, the statistical test of Equation 15 successfully detects all three eruptions, without any false positives (Figure 6a). We note that the detection is not directly related to the retrieved value of the SO_2 flux, nor to the mass at any single distance from the volcano (masses are plotted for $r_n = 25$, 150 and 500 km in Figure 6e). For instance, positive detections are reported for the January 2022 eruption with emission rates as low as 0.4 kton.day^{-1} (2 January 2022), whereas SO_2 rates during non-eruptive periods often exceed this value, but do not lead to any false positives.

Immunity to false positives depends on the robustness of uncertainty estimation. Indeed, in the two repose intervals separating the three eruptions, the mean background SO_2 flux is 0.04 kton.day^{-1}, whereas the mean 1-σ uncertainty is 0.36 kton.day^{-1}, i.e. an order of magnitude larger. Since the criterion of Equation 15 relies on the ratio between these two quantities, it remains consistently negative throughout non-eruptive intervals.

A further illustration of the adaptability of the method is provided by the fortuitous overpass by the plume of the Hunga Tonga–Hunga Ha'apai (HTHH) eruption from 18 to 30 January 2022 (Boichu et al., 2023) (see Figure 7c). At the time it reaches la Réunion, the HTHH plume is diluted, producing a homogeneous non-zero-mean distribution of the SO_2 column amount in the image (Figure 7c1), and a well-marked quadratic component in the mass-to-distance distribution (Figure 7c2). The inversion interprets this pattern as resulting from a higher value of the background noise (up to $\hat{\sigma}_{\mathrm{CA}} = 1.7$ DU), explaining

the sharp increase of posterior uncertainty, reaching an average 0.96 kton.day^{-1} during the overpass (time interval highlighted in magenta in Figure 6b).

In the same vein, periodic fluctuations of pixel noise $\hat{\sigma}_{\mathrm{CA}}$ (peak-to-peak, 0.1–0.3 DU, Figure 6b) are caused by regular introduction of noisy swath-edge rows in the area of interest (noisy stripes in Figure 7a and 7d). Incorporation of these swath-edge rows is a necessary tradeoff to avoid data gaps at low latitudes. The periodicity of $\hat{\sigma}_{\mathrm{CA}}$ results from the progressive drift of Sentinel-5P ground tracks. Even if their distribution is not homogeneous across the image, these noisy observations increase the quadratic term, and the inversion responds by increasing the posterior uncertainty (Figure 7d2). The level of detection is thus momentarily degraded, but it remains possible to analyze moderate to strong degassing patterns that are well above the swath-edge noise (such as the plume displayed in Figure 7a). This strategy avoids repeated interruptions of the time-series, which is valuable for continuously tracking volcanic emissions at low latitudes.

6 Discussion

6.1 Limitations and recommended usage

The "disk method" introduced in this paper relies on a "slender plume approximation" of the atmospheric advection-diffusion equation. The approximation requires that advection (via transport speed u) dominates over along-plume diffusion (D_x). Recasting the "slender plume approximation" in terms of the Péclet number (i.e. $P_e = u^2/D_y k \gg 1$, Section 3.1) places an upper bound on the product kD_x, hence on kD_y (assuming $D_x \approx D_y$, a common simplification made in numerical models of volcanic plume dispersion, e.g. Barsotti et al., 2008; Folch et al., 2009). The extent of the $P_e \gg 1$ domain (or, equivalently, $kD_y \ll u^2$), as a function of k and D_y is represented in Figure S1 for a range of wind speeds.

In summary, according to the "slender plume approximation", either k and D_y should remain "small", or the plume speed u should be "large". Recognizing that k and D_y may be poorly constrained in practice, we here provide general recommendations to adjust the free parameters of the method (CA_{min} and r_{max}) so as to remain within the domain of validity of the assumptions. The choice of the cutoff threshold CA_{min} and maximum integration distance r_{max} is here determined as a compromise between (i) detection threshold for low fluxes and (ii) plausibility of posterior uncertainties.

- **Recommendations for cutoff threshold (CA_{min})**

  In a series of sensitivity experiments on synthetic data (Section 4.2), we observed that, for a given diffusivity D_y and gas loss rate k, increasing the cutoff threshold CA_{min} leads to a progressive underestimation of the gas flux (Fig 3b).

  Tests on real data at Etna (Fig S10) confirm that increasing the cutoff CA_{min} systematically leads to a decrease in the estimated SO_2 fluxes, primarily for the lower fluxes that prevail during inter-eruptive periods (< 1 kton.day^{-1}), which essentially drop to zero when $CA_{min} > 1.0$ DU. Conversely, high fluxes (> 10 kton.day^{-1}) remain stable up to $CA_{min} = 1.4$ DU. However, in turn, since the quadratic term becomes negligible, uncertainties become unacceptably small (down to $\hat{\sigma}_{\mathrm{CA}} = 0.03$ kton.day^{-1}, against a more realistic $\hat{\sigma}_{\mathrm{CA}} = 0.9$ kton.day^{-1} for $CA_{min} = 0.0$ DU).

  We do not recommend using an excessively high CA_{min} in the "disk method". Instead, it is preferable to keep the cutoff threshold CA_{min} to a relatively low value, of the order of the noise level σ_{CA} or even lower (i.e. $CA_{min} \lesssim \sigma_{\mathrm{CA}}$). A low cutoff CA_{min} allows for improving the detection level in presence of moderate to strong gas loss or diffusivity. However, σ_{CA} is not known *a priori*, such that currently CA_{min} needs to be defined by trial-and-error. Future work may focus on identification of representative values for σ_{CA} (hence CA_{min}) depending on the setting, latitude or season. Another strategy could be to exploit ancillary information available in the TROPOMI product.

- **Recommendations for maximum integration distance (r_{max})**

  In previous synthetic explorations of the effect of noise σ_{CA} and wind speed u (Section 4.3), we showed that decreasing the maximum distance of integration r_{max} makes the inversion moderately less vulnerable to gas loss for a fixed wind speed (Figure 3c), but that this benefit is largely overshadowed by the contribution of wind itself (Figure 3d).

  However, tests conducted on real data at Etna show that reducing r_{max} makes the estimation of the spatially-averaged noise $\hat{\sigma}_{\mathrm{CA}}$ less reliable (Fig S11) and likewise of all posterior uncertainties that depend on it. Decreasing the maximum distance r_{max} leads to a systematic decrease of estimated fluxes for the largest emission peaks (paroxysmal events) and a dramatic increase in the estimated uncertainties (from $\hat{\sigma}_{\mathrm{CA}} = 0.9$ kton.day^{-1} for $r_{max} = 1000$ km, increasing to

$\hat{\sigma}_{\mathrm{CA}} = 2.4$ kton.day^{-1} for $r_{max} = 200$ km, and up to $\hat{\sigma}_{\mathrm{CA}} = 5.6$ kton.day^{-1} for $r_{max} = 100$ km).

In summary, following the criterion defined in Section 4.2, the maximum integration distance r_{max} should be as large as possible, as long as it satisfies the condition $r_{max} \lesssim u/k$ (i.e. plume age at r_{max} should be no older than $T = 1/k$).

Unfortunately, k is generally unknown, but in practice, it can be roughly estimated from the ratio between mean wind speed u and the length of a typical plume L_{plume} (i.e. $k \approx u/L_{plume}$). This condition is actually equivalent to setting r_{max} to the length of a typical plume (i.e. $r_{max} \lesssim L_{plume}$), which constitutes a simple rule of thumb.

6.2 Incorporation of information on plume altitude

Thanks to its simplicity, the "disk method" can be efficiently and automatically applied to long time-series. In this study, we assumed a constant plume altitude over long time intervals (1 year at Etna, 2 years at Piton de la Fournaise). Here, the "best" altitude was determined by assessing, *a posteriori*, the agreement between the direction of plume of transport observed in the TROPOMI image (estimated crudely by calculating the coordinates of the center-of-mass of the plume with respect to the source) *versus* the direction of wind predicted by ERA-5. (Figure S6). An example of the agreement between observed and predicted wind direction is shown in Figure 7a and 7b. We note that this consistency only represents a necessary condition, but that it is not sufficient to guarantee that the selected altitude, and thus speed, is correct. Indeed, in the presence of an along-plume vertical wind speed gradient ($\partial u/\partial z$), wind speed may change in the atmospheric column independently of wind direction.

Alternatively, plume altitude could be deduced directly by incorporating information on SO_2 height estimated by advanced retrieval algorithms. This information is present in the standard TROPOMI L2 product (Hedelt et al., 2019), but is restricted to large column amounts (greater than 20 DU). The more sensitive COBRA product proposed recently by Theys et al. (2022) could also provide estimates for lower concentrations, down to 5 DU. Other algorithms exist for the IASI and CrIS infrared sensors (Clarisse et al., 2014; Carboni et al., 2016; Hyman & Pavolonis, 2020), and could be used in synergy. Ability to easily display co-located data from a variety of satellite products, as in the VolcPlume Platform (Boichu & Mathurin, 2022), eases this task.

We also simplified the analysis by incorporating the TROPOMI SO_2 column amount retrieved with an assumption of a plume center-of-mass at 7 km altitude. This choice is in evident contradiction with the selected ERA-5 altitude at Piton de la Fournaise (3 km) and Etna (4.2 km). Alternatively, it is possible to interpolate between SO_2 column amounts retrieved at two different altitudes (e.g. Carn et al., 2013; Theys et al., 2019). Following this logic, we applied a linear interpolation between the flux time-series estimated from the 7 km and 1 km products, which differ by a factor $\sim$ 2–4 (see Figure S7 for Etna and Figure S8 for Piton de la Fournaise). In more complex situations, plume altitude may substantially vary over time, chiefly as a result of variations in the SO_2 flux (see Section 1). In such situations, it would be straightforward to simultaneously adapt the weights of the interpolation, enforcing an on-the-fly consistency with the altitude used in the plume speed normalization, without necessitating further inversion runs. The implementation of the method in an interactive platform (Boichu & Mathurin, 2022) also facilitates manual exploration of the range of plausible altitudes, wind speeds and fluxes, which is convenient for a near-real time analysis.

Several assumptions however limit the generality of the "disk method". The main limitation is the assumption of a simple Gaussian plume, steadily spreading from the source at a constant altitude. In reality, temporal variations in emission strength (and thus, of injection height), combined with variability of wind vectors with altitude and time, often lead to more complex plume shapes. In such situations, the plume may be split in distinct parts (e.g. see Figure 5 of Boichu et al., 2015, at Etna), spread or stagnate close to the source (e.g. see Figure 2 of Behera et al., 2023, at Ambrym), or even be entrained back towards the source due to vorticity of atmospheric transport (e.g. see Figure 2 of Boichu et al., 2014, at Eyjafjallajökul). This is often the case for short-lived, intense periods of degassing, such as syn-eruptive, paroxysmal emissions, where rapid variations in mass flux and altitude often take place. In these situations, it remains possible to restrict the analysis to a short range from the source, where complexity is usually less prevalent (as illustrated in the inset of Figure 7a2). Accordingly, this strategy restricts the inversion to the few hours preceding the satellite acquisition. For more complex cases, it is recommended to apply a more advanced inversion method capable of reconstructing of temporal variations of both SO_2 emission rate and altitude, such as back-trajectory analysis (e.g. Esse et al., 2024) or inverse modeling (e.g. Boichu et al., 2015).

6.3 Lessons learned from application to real cases

The "disk method" has been successfully applied for the estimation of the SO_2 flux released by two volcanoes exhibiting contrasting styles of volcanic activity. At Piton de la Fournaise, the method measures relatively weak fluxes (often < 2 kton.day^{-1}) during three effusive eruptions lasting between 16 and 38 days. Daily fluctuations as low as 0.5 kton.day^{-1} are captured during the July–August 2023 eruption (Figure 5c). Accordingly, these low values cannot be directly generalized into a detection threshold, which largely depends on the level of noise. The actual detection level is expected to be higher in more noisy environments, such as at high latitude (e.g. at Bezymianny, see Supporting Text S1). Nevertheless, the capability of the method to quantify a spatially-averaged pixel noise, without any *a priori*, allows for mapping these uncertainties into realistic error bars on the posterior SO_2 flux. Future efforts could be directed towards a validation of these posterior uncertainties against the precision of column amounts reported in the TROPOMI files. Furthermore, we anticipate that applying the "disk method" to the recently released SO_2 COBRA TROPOMI products will further improve the quality of the results, both in terms of flux and estimated noise (Theys et al., 2021; Fioletov et al., 2023).

The analysis of a two-year-long time series at Piton de la Fournaise also illustrates how the estimation of pixel noise from the "disk method" may be an asset for robustly and automatically detecting degassing events from a target. The three eruptions of 2021–2023 are detected with no false positives, in spite of being associated with low eruptive fluxes. On the other hand, the overpass by the stratospheric Hunga Tonga plume is translated into a temporary increase of the "apparent" background noise, and does not lead to a false increase of the estimated SO_2 flux from Piton de la Fournaise (Section 5.2.3). We also show that the inclusion of noisy swath-edge rows in the data, which is mandatory for providing daily observations without gaps at low latitude, does not substantially impair the results.

Unsurprisingly, by carefully inspecting the cloud fraction and SO_2 flux, we observe that a strong cloud cover leads to an apparent decrease in the SO_2 flux, since low-altitude SO_2 is masked by meteorological clouds. The origin of this bias is traced back to the TROPOMI data, and no simple correction can be applied in post-processing to counter this effect. A pragmatic mitigation strategy may involve discarding estimations for days affected by a

substantial cloud cover (say, $> 50\%$). Fixing a universal threshold for the maximum tolerated cloud cover is not straightforward, as the reliability of the retrieval depends on the signal-to-noise-ratio of the data. Thus, a trial-and-error, case-by-case approach should be preferred. The interactivity offered by the VolcPlume Platform, which provides access to meteorological cloud properties (Boichu & Mathurin, 2022), facilitates this strategy.

More broadly, our analysis outlines a general strategy to leverage the potential of satellite data for the benefit of volcano observatories. Here, we find a reasonable correlation between seismic energy and SO_2 flux, both during short-lived eruptions of Piton de la Fournaise and over longer cycles of paroxysmal sequences at Etna. Systematically comparing SO_2 fluxes and seismic energy is an efficient approach to detect changes in eruption dynamics, while simultaneously allowing for a diagnosis of caveats that may affect remote sensing products.

7 Conclusion

We introduce the "disk method", a novel method to calculate daily volcanic SO_2 flux from TROPOMI imagery. Based on a Gaussian plume model in the "slender plume approximation", a SO_2 "proto-flux" is estimated by a linear regression (as a function of distance) of SO_2 mass integrated in a series of nested circular domains centered on the volcano. Circular integration implies an invariance with respect to the direction of plume transport.

A salient feature of the "disk method" is its ability to jointly quantify the spatially-averaged noise intensity in a satellite image. This allows for deriving robust posterior uncertainties on the SO_2 flux and improving the detection level. To do so, we develop a noise model, considering pixel column amounts as random variables that follow a "truncated normal distribution". We demonstrate that the noise intensity can be estimated from an additional quadratic term in the regression. The noise model is validated experimentally on two datasets affected by noise only. The domain of stability of the inversion with respect to internal atmospheric parameters (gas loss rate, cross-plume diffusivity and wind speed) is constrained from theoretical calculations and sensitivity tests with synthetic and real data.

After completion of the inversion, which is the most computationally-demanding step, information on plume speed can be incorporated by a simple multiplication of wind speed

with the "proto-flux", to deduce the SO_2 flux. The simplicity of this final step makes it straightforward to explore *a posteriori* a range of plume speed scenarios. This way, uncertainty on plume altitude can be efficiently propagated into a range of possible SO_2 fluxes, which represents an additional advantage of the method.

When plume speed is unknown, it can be deduced from global meteorological reanalysis, based on prior knowledge of the plume altitude. Plume altitude can be determined from advanced retrieval algorithms, or by optimizing the agreement between wind direction and the direction of plume transport visible in the satellite images. Here, a fixed ERA-5 pressure level has been used for simplicity, but daily variations of plume altitude, hence speed, could be easily accommodated.

The ratio between estimated SO_2 flux and its posterior uncertainty is exploited in a statistical test to automatically flag occurrences of volcanic degassing. This procedure avoids false positives triggered by fluctuations of noise or intrusion of SO_2 plumes from an external origin.

Application to three eruptions at Piton de la Fournaise (2021–2023) demonstrates that the method allows for capturing small eruptive fluxes (down to ~ 0.5 kton.day^{-1}), while remaining immune to the presence of the diluted stratospheric plume from 2022 Hunga Tonga–Hunga Ha'apai eruption overpassing La Réunion. A one-year-long time-series at Etna (2021) shows that the method allows for measuring the SO_2 flux for a broad range of degassing intensities, from short-lived episodes of paroxysmal activity (with fluxes > 10 kton.day^{-1}) to weeks- to months-long intervals of passive degassing (with fluxes $\sim$ 2–3 kton.day^{-1}). Caveats include the presence of meteorological clouds, which lead to an underestimation of SO_2 abundance by the satellite retrieval. Nevertheless, both at Etna and Piton de la Fournaise, we find a reasonable day-to-day correlation between the SO_2 mass flux estimated by satellite and seismic energy recorded on the ground.

The "disk method" is adapted to derive daily-averaged emission rates from the standard TROPOMI L2 SO_2 product, especially for weakly degassing sources situated in noisy environments. The method has been developed to facilitate automatic processing of large volumes of data, considering (a) that evaluating modest volcanic SO_2 emissions close to the measurement noise is a crucial need for certain applications, especially to capture pre-eruptive fluxes, and (b) that information on local wind velocity and plume altitude is not necessarily available at the time of satellite acquisition. The method is generic, and

readily adaptable to other trace gas observations from TROPOMI or from other UV or IR hyperspectral sensors (IASI, OMI, OMPS).

Implementation of the algorithm as an open-access web app is made available to users at `https://dataviz.icare.univ-lille.fr/so2-flux-calculator`, within the framework of the Volcano Space Observatory Portal (see Supporting Text S5). The app offers interactive features, such as responsive widgets to ease the adjustment of input parameters, and interactive visualization tools to assist human inspection and post-processing. The method is also distributed as an open-source command-line tool in Python language, available from `https://git.icare.univ-lille.fr/icare-public/so2-flux-calculator`. These implementations enable the computation of multi-year time-series, as well as the day-by-day, case-by-case analysis of satellite acquisitions in near-real time, including during the course of an eruption.

Open Research Section

In the framework of the Volcano Space Observatory Portal, the algorithm presented in this paper is implemented in an on-demand web service, available at `https://dataviz.icare.univ-lille.fr/so2-flux-calculator`. The algorithm is also available as a stand-alone open-source Python package at (`https://git.icare.univ-lille.fr/icare-public/so2-flux-calculator`, Grandin et al., 2024b), distributed under MIT Licence. Datasets presented in this paper were generated using the Python implementation of the algorithm. Input and output datasets are available from the Earth System Data Repository (EaSy Data, `https://www.easydata.earth/`, Grandin et al., 2024a). ***Note to reviewers: access to the dataset is currently restricted. The dataset will be released in the public domain when the paper is accepted. The dataset is made available for peer-review as "Data File(s) for Peer Review" (file name: "EaSyData.zip").***

The web-based VOLCPLUME Platform was used for satellite analysis (Boichu & Mathurin, 2022, `https://www.icare.univ-lille.fr/volcplume`). VolcPlume is freely accessible (via `https://volcplume.aeris-data.fr`) and is hosted by AERIS/ICARE Data and Services Centre (`https://www.icare.univ-lille.fr`).

All data used in this study are publicly available:

- Facilities of the European Space Agency (ESA) were used for access to Sentinel-5P TROPOMI Level 2 SO2 products (ESA Copernicus, 2020).
- Facilities of the Copernicus Climate Change Service Climate Data Store (CDS) were used for access to European Centre for Medium-Range Weather Forecasts (ECMWF) ERA-5 global reanalysis (Copernicus Climate Change Service Climate Data Store (CDS), 2023).
- Facilities of the Observatoire Volcanologique du Piton de la Fournaise (OVPF) and Institut de Physique du Globe de Paris (IPGP) were used for access to seismic data acquired at Piton de la Fournaise (Observatoire Volcanologique Du Piton De La Fournaise (OVPF) & Institut De Physique Du Globe De Paris (IPGP), 2008).
- Facilities of the Istituto Nazionale di Geofisica e Vulcanologia (INGV) were used for access to seismic data acquired at Etna (Istituto Nazionale di Geofisica e Vulcanologia (INGV), 2005).

Interactive tools used in the SO_2 Flux Calculator web app are based on libraries of the Holoviz ecosystem (Stevens et al., 2015).

The ObsPy library was used for the processing of seismic data (Krischer et al., 2015). The ssxm.py script was used for computing RSAM (`https://github.com/ThomasLecocq/ssxm/blob/master/ssxm.py`, Lecocq, 2017).

Figure S9, adapted from Chevrel et al. (2023), shows products derived from the MIROVA service (Coppola et al., 2016; Campus et al., 2022) and the HOTVOLC service (Gouhier et al., 2016).

Acknowledgments

Support from AERIS/ICARE Data and Services Centre for the co-development of the VolcPlume web portal, is acknowledged. This project is also supported by FormaTerre (Solid Earth Data and Service centre), by AERIS (Atmosphere Data and Services Centre) and by the Data Terra Research Infrastructure. The FAIR-EASE project gave us the opportunity to develop bridges between data and services coming from the Atmosphere and the Solid Earth communities.

1133 The research was supported by funding from Horizon Europe FAIR-EASE project (grant
1134 No. 101058785) and CaPPA Labex (Agence Nationale de la Recherche No.
1135 ANR-11-LABX-0005-0).

1136 We thank one anonymous Associate Editor, and two anonymous Reviewers for their
1137 insightful comments.

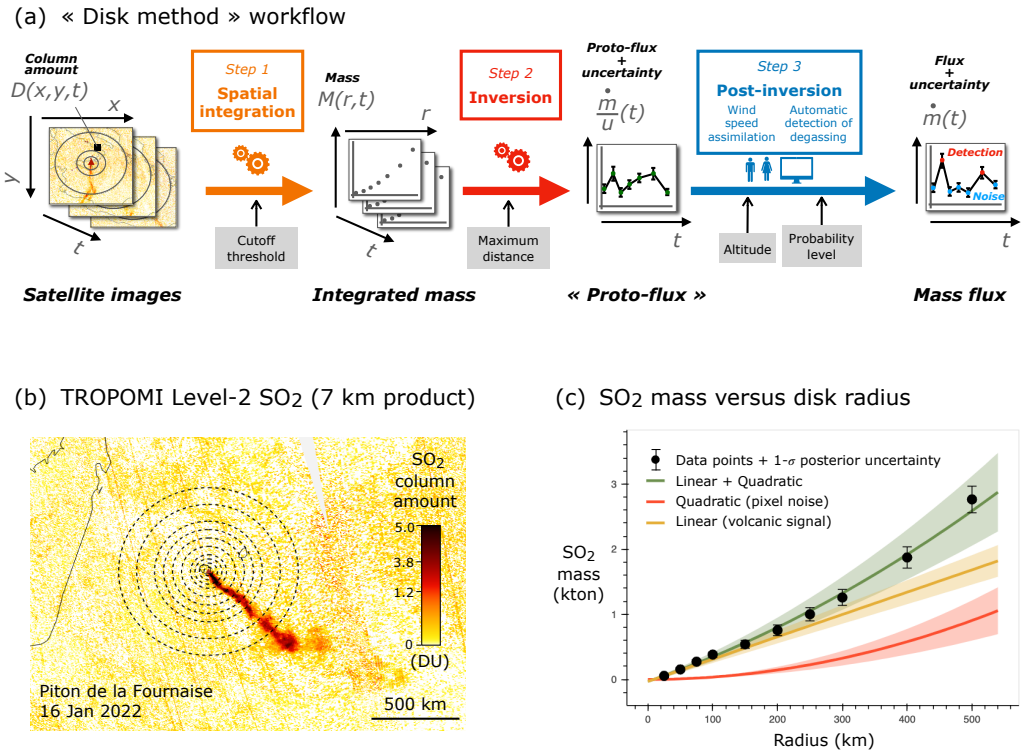

Figure 1. (a) Workflow of the "disk method". (b) Input TROPOMI data. Dashed circles represent the integration domains used in the method (here, up to 500 km radius). (c) Result of inversion of integrated SO_2 masses (black dots) computed by spatial integration over circular domains of the SO_2 column amounts displayed in (b). The yellow line shows the linear "proto-flux" component, proportional to SO_2 flux. The red line represents the quadratic component, resulting from integration of noise. The green line shows the sum of the linear and quadratic components, both estimated from the regression. Posterior uncertainties are represented by colored envelopes.

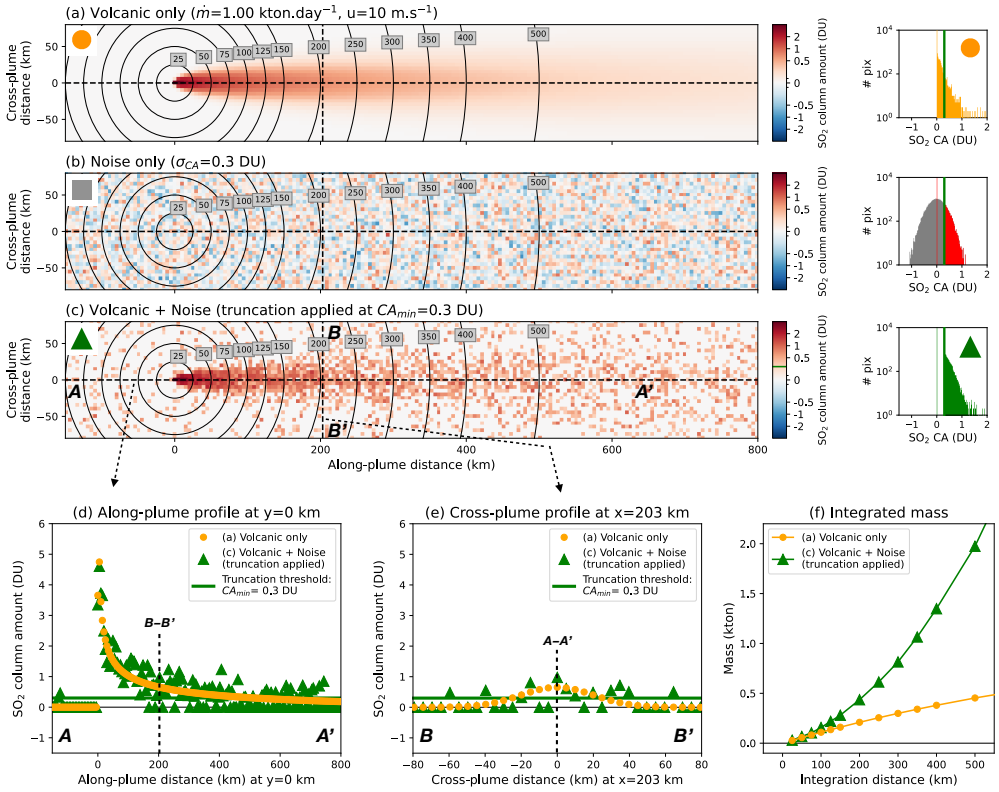

Figure 2. Synthetic TROPOMI images generated from (a) the theoretical "Gaussian plume" model, without noise ($\dot{m}$ = 1.0 kton.day^{-1}; u = 10.0 m.s^{-1}; D_y = 10^4 m^2.s^{-1}; k = 10^{-5} s^{-1}), (b) noise only (zero-mean normally distributed noise, with σ_{CA}=0.3 DU) and (c) sum of the plume model in (a) and the noise model in (b), followed by truncation of column amounts smaller than CA_{min}. Histograms to the right show the distribution of column amounts in each image. Red part of histogram in (b) shows the fraction of the noise population situated above the cutoff CA_{min}=0.3 DU (vertical green line). (d) Along-plume profile ***A***-***A***' across the core of the plume for column amounts in (a)–(c). (e) Cross-plume profile ***B***-***B***' at 203 km from the source. (f) Integrated mass, as a function of distance from source, calculated from the synthetic images of (a) and (c). Domains of integrations are centered on the volcano and are represented by circles in (a) and (c).

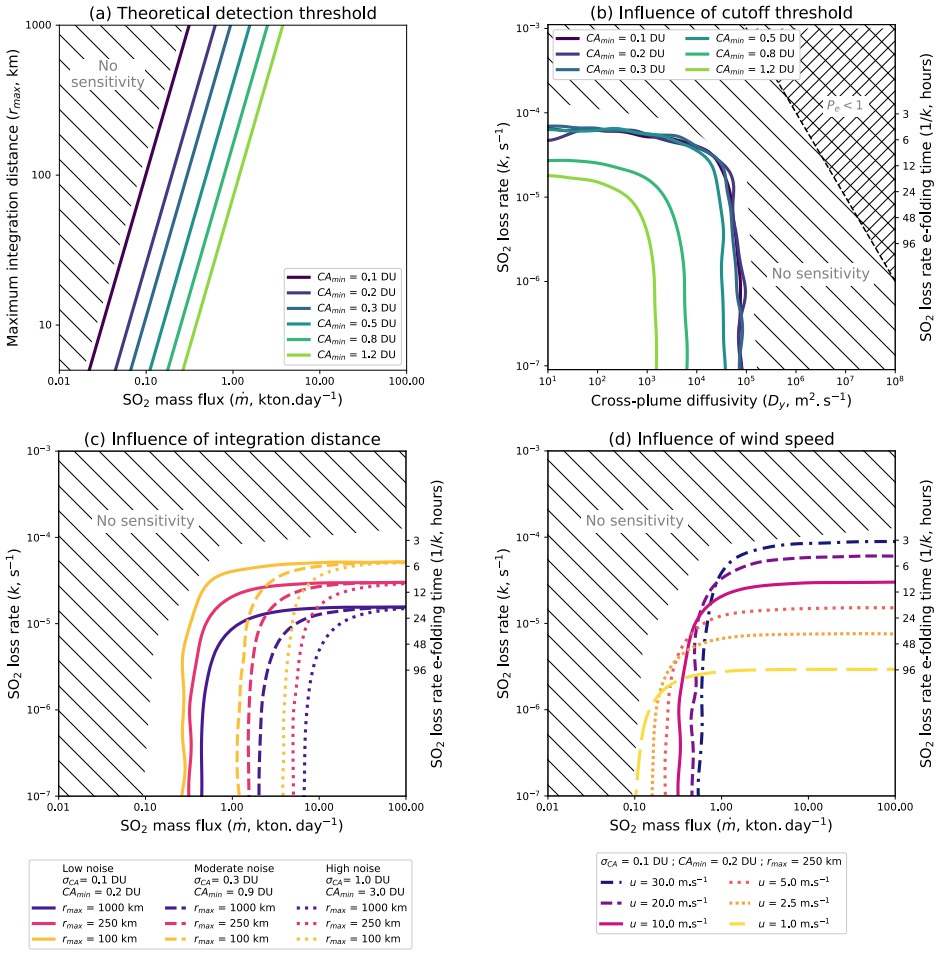

Figure 3. Sensitivity of the inversion scheme. In all panels, hatched area represents the domain where sensitivity to SO_2 emissions falls to zero. (a) Theoretical lower bound for detectable mass flux $\dot{m}$ (x-axis), as a function of integration distance r_{max} (y-axis) and cutoff threshold CA_{min} (colored lines), for a scenario with no gas loss, no noise, fixed wind speed and diffusivity (respectively, u=10 m.s^{-1} and D_y=10^4 m^2.s^{-1}). See Supporting Text S4 for details. (b) Experimental exploration of the influence of cutoff threshold CA_{min} (colored contours) on the domain sensitivity, represented as a function of diffusivity D_y (x-axis) and gas loss rate k (y-axis), for a scenario with fixed values of mass flux, wind speed, noise and maximum distance of integration (respectively, $\dot{m}$=1 kton.day^{-1}, u=10 m.s^{-1}, σ_{CA}=0.3 DU and r_{max}=500 km). Individual plots are shown in Figure S2. (c) Experimental exploration of detection threshold $\dot{m}$ (x-axis) as a function of gas loss rate k (y-axis) for scenarios corresponding to "low noise" (solid curve), "moderate noise" (dashed curve) and "high noise" (dotted curve), for a fixed diffusivity (D_y=10^4 m^2.s^{-1}). In each scenario, three values of the maximum distance of integration r_{max} are explored (blue: 1000 km; red: 250 km; yellow: 100 km). Individual plots are shown in Figure S3. (d) Same as (d), for a scenario with all parameters fixed (σ_{CA}=0.1 DU, CA_{min}=0.2 DU, r_{max}=250 km, D_y=10^4 m^2.s^{-1}), except wind speed u (colored curves). Individual plots are shown in Figure S4.

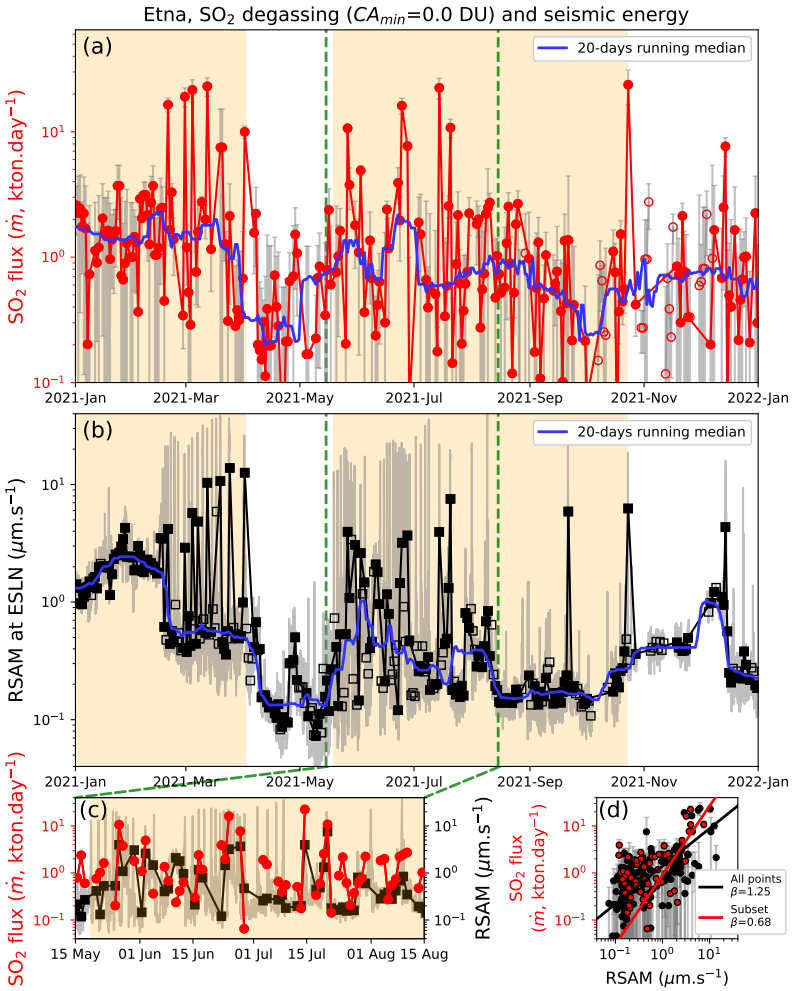

Figure 4. (a) SO_2 flux from TROPOMI at Etna volcano for the year 2021. Error bars represent the 1-σ posterior uncertainties on SO_2 flux. (b) Real-time seismic amplitude (RSAM) at ESLN seismometer. Grey lines represent the raw RSAM record, whereas black lines show time-averaged RSAM in the 8 hours preceding TROPOMI acquisitions (see Section 2.2). Solid symbols represent daily measurements when both SO_2 flux and RSAM records are available. Otherwise, an empty symbol is used. Blue lines are 20-days running averages. The two paroxysmal sequences of 2021 (PS1 and PS2, as defined by Aiuppa et al., 2015) are highlighted in orange. (c) RSAM and SO_2 flux at Etna for a period of repeated lava fountain events (15 May 2021 – 15 August 2021). (d) Daily RSAM (x-axis) *versus* SO_2 flux (y-axis). The best-fitting power law ($y = a.x^{1/\beta}$) is shown by a red line for the subset of points in (c), and a black line for all points in the 1-year time-series.

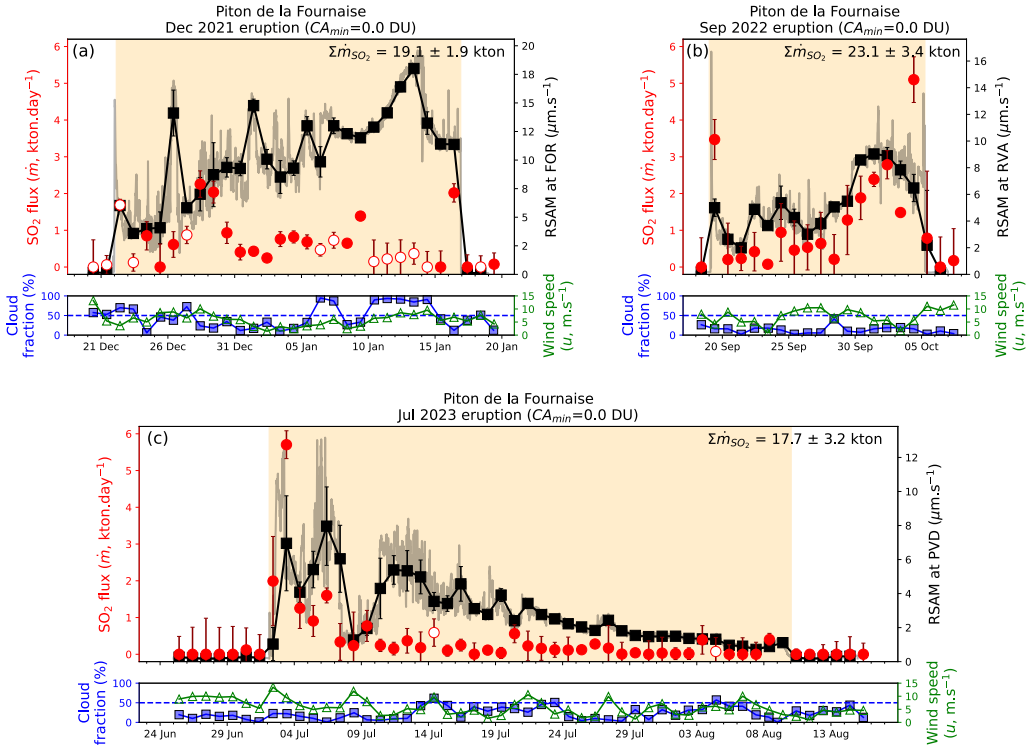

Figure 5. Comparison of daily estimations of syn-eruptive SO_2 mass flux derived from TROPOMI (red circles, with associated 1-σ uncertainties shown by red error bars) *versus* RSAM (black squares) for three eruptions of Piton de la Fournaise: (a) December 2021 – January 2022 eruption (duration 25 days), (b) September 2022 – October 2022 eruption (duration 16 days), (c) July 2023 – August 2023 eruption (duration 38 days). SO_2 estimations for cloud fraction greater than 50% are indicated by white-filled symbols. Blue and green curves in lower panels represent the cloud fraction and ERA-5 wind speed, respectively. For RSAM, grey lines represent the raw RSAM record, black lines show time-averaged RSAM in the 5 hours preceding TROPOMI acquisitions and error bars show the 1-σ standard deviation of RSAM in the 5 hours time-window (see Section 2.2).

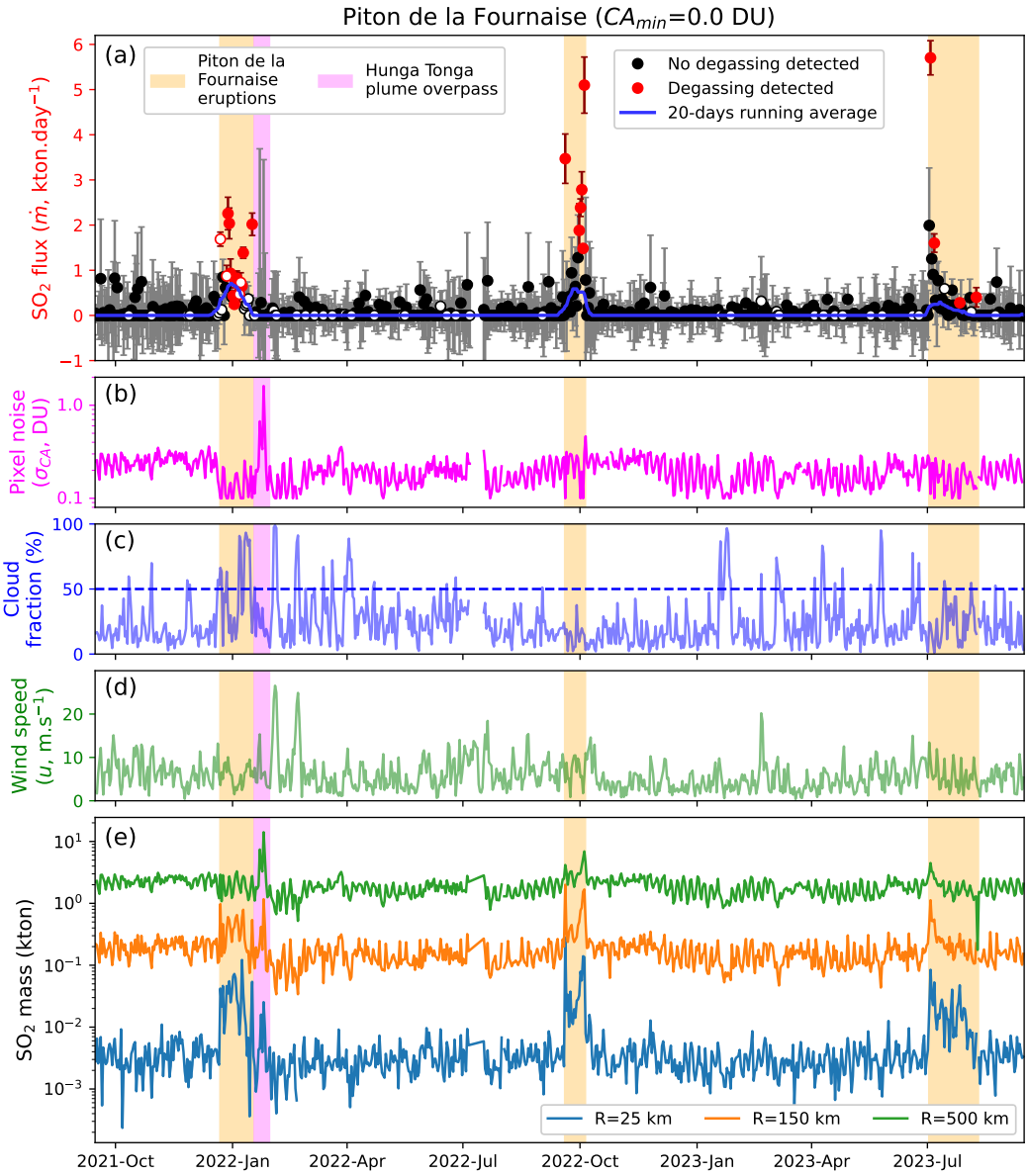

Figure 6. (a) SO_2 mass flux deduced from the mass time-series for $R \leq 500$ km. Red dots show dates that passed the statistical test of Equation 15, i.e. indicating a positive detection of degassing (confidence level: 99%). Error bars (in grey or dark red) represent 1-σ posterior uncertainties. Blue line is the 20-days running average. White-filled symbols correspond to cloud fraction $> 50\%$. (b) Estimated 1-σ spatially-averaged pixel noise $\hat{\sigma}_{\mathrm{CA}}$. (c) Cloud fraction. (d) ERA-5 wind speed at 700 hPa. (e) SO_2 mass integrated for three radii (25, 150 and 500 km) around Piton de la Fournaise, computed with CA_{min}=0.0 DU. Time intervals highlighted in orange mark the three latest eruptions of Piton de la Fournaise. Area highlighted in magenta shows the overpass by the stratospheric Hunga Tonga Hunga Ha'apai (HT-HH) eruption plume (eruption date: 15 January 2022, see also Figure 7).

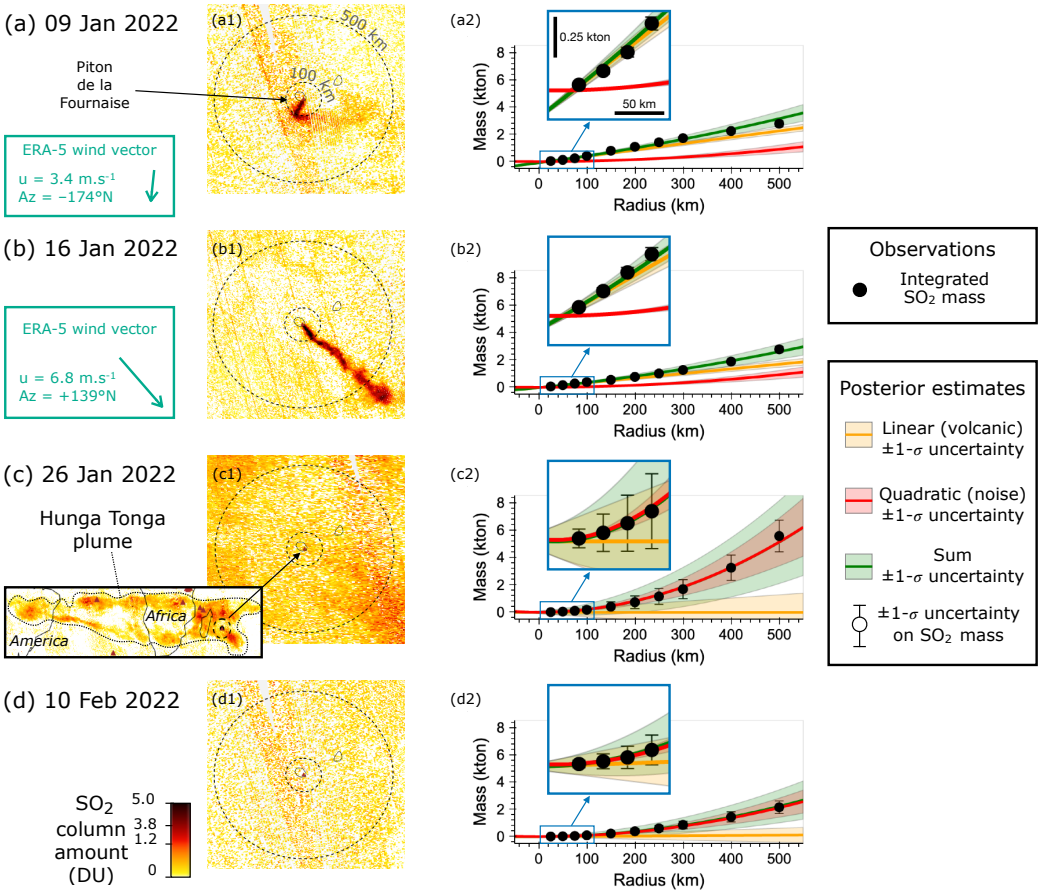

Figure 7. Left: TROPOMI SO_2 column amount around Piton de la Fournaise (a-b) during the January 2022 eruption, (c) after eruption end and during overpass by the Hunga Tonga Hunga Ha'apai (HTHH) plume, and (d) after HTHH plume overpass. The blue arrows for the eruptive cases (a1) and (b1) show the wind vectors deduced from ERA-5 (700 hPa pressure level), which are consistent with the direction taken by the plume. Right: best-fitting mass-*versus*-distance regression for the data points derived from integration of SO_2 mass over disks (black dots). Line colors are the same as in Figure 1 (yellow: volcanic; red: noise; green: sum). For each plot, the inset shows a zoom on the four data points within 100 km from the volcano.

References

Aiuppa, A., Lo Bue Trisciuzzi, G., Alparone, S., Bitetto, M., Coltelli, M., Delle Donne, D., ... Pecora, E. (2023). A SO_2 flux study of the Etna volcano 2020–2021 paroxysmal sequences. *Frontiers in Earth Science*, *11*, 1115111.

Aiuppa, A., et al. (2015). Volcanic-gas monitoring. In *Volcanism and global environmental change* (pp. 81–96). Cambridge University Press.

Andres, R., & Schmid, J. (2001). The effects of volcanic ash on COSPEC measurements. *Journal of Volcanology and Geothermal Research*, *108*(1-4), 237–244.

Arellano, S., Galle, B., Apaza, F., Avard, G., Barrington, C., Bobrowski, N., ... others (2021). Synoptic analysis of a decade of daily measurements of SO_2 emission in the troposphere from volcanoes of the global ground-based Network for Observation of Volcanic and Atmospheric Change. *Earth System Science Data*, *13*(3), 1167–1188.

Aubry, T. J., Engwell, S. L., Bonadonna, C., Mastin, L. G., Carazzo, G., Van Eaton, A. R., ... others (2023). New insights into the relationship between mass eruption rate and volcanic column height based on the ivespa data set. *Geophysical Research Letters*, *50*(14), e2022GL102633.

Barr, S., & Gifford, F. A. (1987). The random force theory applied to regional scale tropospheric diffusion. *Atmospheric Environment (1967)*, *21*(8), 1737–1741.

Barsotti, S., Neri, A., & Scire, J. (2008). The VOL-CALPUFF model for atmospheric ash dispersal: 1. Approach and physical formulation. *Journal of Geophysical Research: Solid Earth*, *113*(B3).

Battaglia, J., Aki, K., & Staudacher, T. (2005). Location of tremor sources and estimation of lava output using tremor source amplitude on the Piton de la Fournaise volcano: 2. Estimation of lava output. *Journal of volcanology and geothermal research*, *147*(3-4), 291–308.

Behera, A. K., Boichu, M., Thieuleux, F., Henriot, N., & Hioki, S. (2023). Strength of TROPOMI satellite observations in retrieving hourly resolved sources of volcanic sulfur dioxide by inverse modeling. *EGUsphere*, *2023*, 1–31. Retrieved from `https://egusphere.copernicus.org/preprints/2023/egusphere-2023-2545/` doi: 10.5194/egusphere-2023-2545

Beirle, S., Hörmann, C., Penning de Vries, M., Dörner, S., Kern, C., & Wagner, T. (2014). Estimating the volcanic emission rate and atmospheric lifetime of SO_2 from space: A case study for Kīlauea Volcano, Hawaii. *Atmospheric Chemistry and Physics*,

14(16), 8309–8322.

Boichu, M., Clarisse, L., Khvorostyanov, D., & Clerbaux, C. (2014). Improving volcanic sulfur dioxide cloud dispersal forecasts by progressive assimilation of satellite observations. *Geophysical Research Letters*, *41*(7), 2637–2643. doi: 10.1002/2014GL059496

Boichu, M., Clarisse, L., Péré, J.-C., Herbin, H., Goloub, P., Thieuleux, F., ... Tanré, D. (2015). Temporal variations of flux and altitude of sulfur dioxide emissions during volcanic eruptions: implications for long-range dispersal of volcanic clouds. *Atmospheric Chemistry and Physics*, *15*(14), 8381–8400. doi: 10.5194/acp-15-8381-2015

Boichu, M., Grandin, R., Blarel, L., Torres, B., Derimian, Y., Goloub, P., ... Riedi, J. (2023). Growth and Global Persistence of Stratospheric Sulfate Aerosols From the 2022 Hunga Tonga–Hunga Ha'apai Volcanic Eruption. *Journal of Geophysical Research: Atmospheres*, *128*(23), e2023JD039010. Retrieved from `https://agupubs.onlinelibrary.wiley.com/doi/abs/10.1029/2023JD039010` (e2023JD039010 2023JD039010) doi: https://doi.org/10.1029/2023JD039010

Boichu, M., & Mathurin, T. (2022). *VOLCPLUME, an interactive web portal for the multiscale analysis of volcanic plume physico-chemical properties. [Interactive Web based Ressource], AERIS.* Retrieved from `https://volcplume.aeris-data.fr/` (Website address: `https://www.icare.univ-lille.fr/volcplume/`) doi: 10.25326/362

Boichu, M., Menut, L., Khvorostyanov, D., Clarisse, L., Clerbaux, C., Turquety, S., & Coheur, P.-F. (2013). Inverting for volcanic SO_2 flux at high temporal resolution using spaceborne plume imagery and chemistry-transport modelling: the 2010 Eyjafjallajökull eruption case study. *Atmospheric Chemistry and Physics*, *13*(17), 8569–8584. doi: 10.5194/acp-13-8569-2013

Brenot, H., Theys, N., Clarisse, L., Van Geffen, J., Van Gent, J., Van Roozendael, M., ... others (2014). Support to Aviation Control Service (SACS): an online service for near-real-time satellite monitoring of volcanic plumes. *Natural Hazards and Earth System Sciences*, *14*(5), 1099–1123.

Cai, Z., Griessbach, S., & Hoffmann, L. (2021). Improved estimation of volcanic SO_2 injections from satellite observations and Lagrangian transport simulations: the 2019 Raikoke eruption. *Atmospheric Chemistry & Physics Discussions*.

Campus, A., Laiolo, M., Massimetti, F., & Coppola, D. (2022). The transition from modis to viirs for global volcano thermal monitoring. *Sensors*, *22*(5), 1713.

Carboni, E., Grainger, R. G., Mather, T. A., Pyle, D. M., Thomas, G. E., Siddans, R., ... Balis, D. (2016). The vertical distribution of volcanic SO_2 plumes measured by IASI. *Atmospheric Chemistry and Physics*, *16*(7), 4343–4367.

Carboni, E., Mather, T. A., Schmidt, A., Grainger, R. G., Pfeffer, M. A., Ialongo, I., & Theys, N. (2019). Satellite-derived sulfur dioxide (SO_2) emissions from the 2014–2015 Holuhraun eruption (Iceland). *Atmospheric Chemistry and Physics*, *19*(7), 4851–4862.

Carn, S. A., Clarisse, L., & Prata, A. J. (2016). Multi-decadal satellite measurements of global volcanic degassing. *Journal of Volcanology and Geothermal Research*, *311*, 99–134.

Carn, S. A., Fioletov, V. E., McLinden, C. A., Li, C., & Krotkov, N. A. (2017). A decade of global volcanic SO_2 emissions measured from space. *Scientific reports*, *7*(1), 44095.

Carn, S. A., Krotkov, N., Yang, K., & Krueger, A. (2013). Measuring global volcanic degassing with the Ozone Monitoring Instrument (OMI). *Geological Society, London, Special Publications*, *380*(1), 229–257.

Carn, S. A., Krueger, A. J., Bluth, G., Schaefer, S., Krotkov, N., Watson, I., & Datta, S. (2003). Volcanic eruption detection by the Total Ozone Mapping Spectrometer (TOMS) instruments: A 22-year record of sulphur dioxide and ash emissions. *Geological Society, London, Special Publications*, *213*(1), 177–202.

Chevrel, M. O., Villeneuve, N., Grandin, R., Froger, J.-L., Coppola, D., Massimetti, F., ... Peltier, A. (2023). Lava flow daily monitoring: the case of the 19 September–5 October 2022 eruption at Piton de la Fournaise. *Volcanica*, *6*(2), 391–404. doi: 10.30909/vol.06.02.391404

Clarisse, L., Coheur, P.-F., Theys, N., Hurtmans, D., & Clerbaux, C. (2014). The 2011 Nabro eruption, a SO_2 plume height analysis using IASI measurements. *Atmospheric chemistry and physics*, *14*(6), 3095–3111.

Copernicus Climate Change Service Climate Data Store (CDS). (2023). *ERA5 hourly data on single levels from 1940 to present [Dataset].* Copernicus Climate Change Service Climate Data Store (CDS). Retrieved from `https://cds.climate.copernicus.eu/cdsapp#!/dataset/`

reanalysis-era5-single-levels?tab=overview doi: 10.24381/cds.adbb2d47

Coppola, D., Laiolo, M., Cigolini, C., Donne, D. D., & Ripepe, M. (2016). Enhanced volcanic hot-spot detection using modis ir data: results from the mirova system. *Geological Society, London, Special Publications*, *426*(1), 181–205.

Coppola, D., Laiolo, M., Massimetti, F., & Cigolini, C. (2019). Monitoring endogenous growth of open-vent volcanoes by balancing thermal and SO_2 emissions data derived from space. *Scientific reports*, *9*(1), 9394.

Corradini, S., Guerrieri, L., Brenot, H., Clarisse, L., Merucci, L., Pardini, F., ... Theys, N. (2021). Tropospheric volcanic SO_2 mass and flux retrievals from satellite. The Etna December 2018 eruption. *Remote Sensing*, *13*(11), 2225.

Corradini, S., Guerrieri, L., Stelitano, D., Salerno, G., Scollo, S., Merucci, L., ... others (2020). Near real-time monitoring of the Christmas 2018 Etna eruption using SEVIRI and products validation. *Remote Sensing*, *12*(8), 1336.

Delle Donne, D., Aiuppa, A., Bitetto, M., D'Aleo, R., Coltelli, M., Coppola, D., ... Tamburello, G. (2019). Changes in SO_2 flux regime at Mt. Etna captured by automatically processed ultraviolet camera data. *Remote Sensing*, *11*(10), 1201.

Dumont, Q., Cayol, V., Froger, J.-L., & Peltier, A. (2022). 22 years of satellite imagery reveal a major destabilization structure at Piton de la Fournaise. *Nature Communications*, *13*(1), 2649.

Eckhardt, S., Prata, A., Seibert, P., Stebel, K., & Stohl, A. (2008). Estimation of the vertical profile of sulfur dioxide injection into the atmosphere by a volcanic eruption using satellite column measurements and inverse transport modeling. *Atmospheric Chemistry and Physics*, *8*(14), 3881–3897.

Endo, E. T., & Murray, T. (1991). Real-time seismic amplitude measurement (RSAM): a volcano monitoring and prediction tool. *Bulletin of Volcanology*, *53*, 533–545.

ESA Copernicus. (2020). *Sentinel-5P TROPOMI Level 2 Sulphur Dioxide Total Column. Version 02. [Dataset].* Retrieved from https://documentation.dataspace.copernicus.eu/Data/SentinelMissions/Sentinel5P.html#sentinel-5p-level-2-sulfur-dioxide doi: 10.5270/S5P-74eidii

Esse, B., Burton, M., Hayer, C., Contreras-Arratia, R., Christopher, T., Joseph, E. P., ... Johnson, C. (2024). SO_2 emissions during the 2021 eruption of La Soufrière, St Vincent, revealed with back-trajectory analysis of TROPOMI imagery. *Geological*

Society, London, Special Publications, *539*(1), 231–244.

Fioletov, V. E., McLinden, C., Griffin, D., Abboud, I., Krotkov, N., Leonard, P. J. T., ... Carn, S. (2022). *Multi-Satellite Air Quality Sulfur Dioxide (SO2) Database Long-Term L4 Global V2 [Dataset].* Goddard Earth Science Data and Information Services Center (GES DISC). Retrieved from `https://so2.gsfc.nasa.gov/kml/Catalogue_SO2_2022.xls` doi: 10.5067/MEASURES/SO2/DATA406

Fioletov, V. E., McLinden, C. A., Griffin, D., Abboud, I., Krotkov, N., Leonard, P. J. T., ... Carn, S. (2023). Version 2 of the global catalogue of large anthropogenic and volcanic SO_2 sources and emissions derived from satellite measurements. *Earth System Science Data*, *15*(1), 75–93.

Fioletov, V. E., McLinden, C. A., Griffin, D., Theys, N., Loyola, D. G., Hedelt, P., ... Li, C. (2020). Anthropogenic and volcanic point source SO_2 emissions derived from TROPOMI on board Sentinel-5 Precursor: first results. *Atmospheric Chemistry and Physics*, *20*(9), 5591–5607.

Fioletov, V. E., McLinden, C. A., Krotkov, N., Li, C., Joiner, J., Theys, N., ... Moran, M. D. (2016). A global catalogue of large SO_2 sources and emissions derived from the Ozone Monitoring Instrument. *Atmospheric Chemistry and Physics*, *16*(18), 11497–11519.

Flemming, J., & Inness, A. (2013). Volcanic sulfur dioxide plume forecasts based on UV satellite retrievals for the 2011 Grímsvötn and the 2010 Eyjafjallajökull eruption. *Journal of Geophysical Research: Atmospheres*, *118*(17), 10–172.

Folch, A., Costa, A., & Macedonio, G. (2009). FALL3D: A computational model for transport and deposition of volcanic ash. *Computers & Geosciences*, *35*(6), 1334–1342.

Girault, F., Carazzo, G., Tait, S., Ferrucci, F., & Kaminski, É. (2014). The effect of total grain-size distribution on the dynamics of turbulent volcanic plumes. *Earth and Planetary Science Letters*, *394*, 124–134.

Girona, T., Costa, F., Newhall, C., & Taisne, B. (2014). On depressurization of volcanic magma reservoirs by passive degassing. *Journal of Geophysical Research: Solid Earth*, *119*(12), 8667–8687.

Giuffrida, M., Cardone, M., Zuccarello, F., & Viccaro, M. (2023). Etna 2011–2022: Discoveries from a decade of activity at the volcano. *Earth-Science Reviews*, 104563.

Global Volcanism Program. (2021). *Etna (Italy) Frequent explosions, ash plumes, fountaining, and lava flows during December 2020–March 2021* (Bulletin of the Global Volcanism Network No. 46:4). Piazza Roma, 2 - 95125 Catane, Italy: Smithsonian Institution. Retrieved from `https://volcano.si.edu/showreport.cfm?doi=10.5479/si.GVP.BGVN202104-211060` doi: 10.5479/si.GVP.BGVN202104-211060

Gouhier, M., Guéhenneux, Y., Labazuy, P., Cacault, P., Decriem, J., & Rivet, S. (2016). Hotvolc: A web-based monitoring system for volcanic hot spots. *Geological Society, London, Special Publications*, *426*(1), 223–241.

Grandin, R., Boichu, M., Mathurin, T., & Pascal, N. (2024a). *SO_2 Flux Calculator input and output data [Dataset].* Retrieved from `\url{https://www.easydata.earth/}` (Access currently restricted)

Grandin, R., Boichu, M., Mathurin, T., & Pascal, N. (2024b). *SO_2 Flux Calculator [Software].* Retrieved from `https://git.icare.univ-lille.fr/icare-public/so2-flux-calculator`

Hayer, C., Burton, M., Ferrazzini, V., Esse, B., & Di Muro, A. (2023). Unusually high SO_2 emissions and plume height from Piton de la Fournaise volcano during the April 2020 eruption. *Bulletin of Volcanology*, *85*(4), 21.

Hedelt, P., Efremenko, D. S., Loyola, D. G., Spurr, R., & Clarisse, L. (2019). Sulfur dioxide layer height retrieval from Sentinel-5 Precursor/TROPOMI using FP_ILM. *Atmospheric Measurement Techniques*, *12*(10), 5503–5517.

Heng, Y., Hoffmann, L., Griessbach, S., Rößler, T., & Stein, O. (2016). Inverse transport modeling of volcanic sulfur dioxide emissions using large-scale simulations. *Geoscientific model development*, *9*(4), 1627–1645.

Hersbach, H., Bell, B., Berrisford, P., Hirahara, S., Horányi, A., Muñoz-Sabater, J., ... Thépaut, J.-N. (2020). The ERA5 global reanalysis. *Quarterly Journal of the Royal Meteorological Society*, *146*(730), 1999–2049.

Hibert, C., Mangeney, A., Polacci, M., Muro, A. D., Vergniolle, S., Ferrazzini, V., ... others (2015). Toward continuous quantification of lava extrusion rate: Results from the multidisciplinary analysis of the 2 January 2010 eruption of Piton de la Fournaise volcano, La Réunion. *Journal of Geophysical Research: Solid Earth*, *120*(5), 3026–3047.

Hughes, E. J., Sparling, L., Carn, S., & Krueger, A. (2012). Using horizontal transport characteristics to infer an emission height time series of volcanic SO_2. *Journal of Geophysical Research: Atmospheres*, *117*(D18).

Hyman, D. M., & Pavolonis, M. J. (2020). Probabilistic retrieval of volcanic SO_2 layer height and partial column density using the Cross-track Infrared Sounder (CrIS). *Atmospheric Measurement Techniques*, *13*(11), 5891–5921.

Hyman, D. M., Pavolonis, M. J., & Sieglaff, J. (2021). A novel approach to estimating time-averaged volcanic so_2 fluxes from infrared satellite measurements. *Remote Sensing*, *13*(5), 966.

Ichihara, M. (2016). Seismic and infrasonic eruption tremors and their relation to magma discharge rate: A case study for sub-Plinian events in the 2011 eruption of Shinmoe-dake, Japan. *Journal of Geophysical Research: Solid Earth*, *121*(10), 7101–7118.

INGV. (2021a). *Etna Weekly report, 15 February 2021 – 21 February 2021* (Istituto Nazionale di Geofisica e Vulcanologia (INGV) report No. 08/2021). Piazza Roma, 2 - 95125 Catane, Italy: Sezioni di Catania e Palermo. Retrieved from `https://www.ct.ingv.it/index.php/monitoraggio-e-sorveglianza/prodotti-del-monitoraggio/bollettini-settimanali-multidisciplinari/473-bollettino-settimanale-sul-monitoraggio-vulcanico-geochimico-e-sismico-del-vulcano-etna20210223/file`

INGV. (2021b). *Etna Weekly report, 21 June 2021 – 27 June 2021* (Istituto Nazionale di Geofisica e Vulcanologia (INGV) report No. 26/2021). Piazza Roma, 2 - 95125 Catane, Italy: Sezioni di Catania e Palermo. Retrieved from `https://www.ct.ingv.it/index.php/monitoraggio-e-sorveglianza/prodotti-del-monitoraggio/bollettini-settimanali-multidisciplinari/515-bollettino-settimanale-sul-monitoraggio-vulcanico-geochimico-e-sismico-del-vulcano-etna20210629/file`

Istituto Nazionale di Geofisica e Vulcanologia (INGV). (2005). *Rete Sismica Nazionale (RSN) [Dataset].* Istituto Nazionale di Geofisica e Vulcanologia (INGV). Retrieved from `http://terremoti.ingv.it/instruments/network/IV` doi: 10.13127/SD/X0FXNH7QFY

Johnson, N. L., Kotz, S., & Balakrishnan, N. (1994). *Continuous univariate distributions, 2nd edition* (Vol. 1). John Wiley & sons.

Joseph, E., Camejo-Harry, M., Christopher, T., Contreras-Arratia, R., Edwards, S., Graham, O., ... Sparks, R. S. J. (2022). Responding to eruptive transitions during the 2020–2021 eruption of La Soufrière volcano, St. Vincent. *Nature Communications*, *13*(1), 4129.

Journeau, C., Shapiro, N. M., Peltier, A., Ferrazzini, V., Soubestre, J., Duputel, Z., ... Coppola, D. (2023). Tracking changes in the co-eruptive seismic tremor associated with magma degassing at Piton de la Fournaise volcano. *Journal of Volcanology and Geothermal Research*, *444*, 107936.

Kern, C., Deutschmann, T., Werner, C., Sutton, A. J., Elias, T., & Kelly, P. J. (2012). Improving the accuracy of SO_2 column densities and emission rates obtained from upward-looking UV-spectroscopic measurements of volcanic plumes by taking realistic radiative transfer into account. *Journal of Geophysical Research: Atmospheres*, *117*(D20).

Kern, C., Lerner, A. H., Elias, T., Nadeau, P. A., Holland, L., Kelly, P. J., ... Cappos, M. (2020). Quantifying gas emissions associated with the 2018 rift eruption of Kīlauea Volcano using ground-based DOAS measurements. *Bulletin of Volcanology*, *82*(7), 55.

Khokhar, M., Frankenberg, C., Van Roozendael, M., Beirle, S., Kühl, S., Richter, A., ... Wagner, T. (2005). Satellite observations of atmospheric SO_2 from volcanic eruptions during the time-period of 1996–2002. *Advances in Space Research*, *36*(5), 879–887.

Kilbride, B. M., Edmonds, M., & Biggs, J. (2016). Observing eruptions of gas-rich compressible magmas from space. *Nature Communications*, *7*(1), 13744.

Krischer, L., Megies, T., Barsch, R., Beyreuther, M., Lecocq, T., Caudron, C., & Wassermann, J. (2015). Obspy: A bridge for seismology into the scientific python ecosystem. *Computational Science & Discovery*, *8*(1), 014003.

Kristiansen, N., Stohl, A., Prata, A., Richter, A., Eckhardt, S., Seibert, P., ... Stebel, K. (2010). Remote sensing and inverse transport modeling of the Kasatochi eruption sulfur dioxide cloud. *Journal of Geophysical Research: Atmospheres*, *115*(D2).

Krueger, A., Schnetzler, C., & Walter, L. (1996). The December 1981 eruption of Nyamuragira volcano (Zaire), and the origin of the "mystery cloud" of early 1982. *Journal of Geophysical Research: Atmospheres*, *101*(D10), 15191–15196.

Lecocq, T. (2017). *RSAM function for ObsPy [Software].* Retrieved from

https://github.com/ThomasLecocq/ssxm/blob/master/ssxm.py

Lopez, T., Carn, S., Werner, C., Fee, D., Kelly, P., Doukas, M., ... Schneider, D. (2013). Evaluation of Redoubt Volcano's sulfur dioxide emissions by the Ozone Monitoring Instrument. *Journal of Volcanology and Geothermal Research*, *259*, 290–307.

Loughlin, S. C., Sparks, R. S. J., Brown, S. K., Jenkins, S. F., & Vye-Brown, C. (2015). *Global volcanic hazards and risk*. Cambridge University Press.

Markus, B., Valade, S., Wöllhaf, M., & Hellwich, O. (2023). Automatic retrieval of volcanic SO_2 emission source from TROPOMI products. *Frontiers in Earth Science*, *10*, 1064171. Retrieved from

\url{https://github.com/bazsimarkus/tropomi-emission-source}

Marshall, L. R., Maters, E. C., Schmidt, A., Timmreck, C., Robock, A., & Toohey, M. (2022). Volcanic effects on climate: recent advances and future avenues. *Bulletin of Volcanology*, *84*(5), 54.

Mastin, L. G., Guffanti, M., Servranckx, R., Webley, P., Barsotti, S., Dean, K., ... Waythomas, C. (2009). A multidisciplinary effort to assign realistic source parameters to models of volcanic ash-cloud transport and dispersion during eruptions. *Journal of Volcanology and Geothermal Research*, *186*(1-2), 10–21.

McCormick, B. T., Edmonds, M., Mather, T. A., Campion, R., Hayer, C. S., Thomas, H. E., & Carn, S. A. (2013). Volcano monitoring applications of the ozone monitoring instrument. *Geological Society, London, Special Publications*, *380*(1), 259–291.

Merucci, L., Burton, M., Corradini, S., & Salerno, G. G. (2011). Reconstruction of SO_2 flux emission chronology from space-based measurements. *Journal of Volcanology and Geothermal Research*, *206*(3-4), 80–87.

Météo-France. (2021, December). *Monthly Climatological Bulletin, La Réunion, December 2021* (Tech. Rep.). 50, Bd du Chaudron, 97490 Ste-Clotilde, La Réunion: Direction Inter Régionale Océan Indien. Retrieved from

https://donneespubliques.meteofrance.fr/donnees_libres/bulletins/BCMOM/BCMOM_974_202112.pdf

Météo-France. (2022a, January). *Monthly Climatological Bulletin, La Réunion, January 2022* (Tech. Rep.). 50, Bd du Chaudron, 97490 Ste-Clotilde, La Réunion: Direction Inter Régionale Océan Indien. Retrieved from

https://donneespubliques.meteofrance.fr/donnees_libres/bulletins/BCMOM/

BCMOM_974_202201.pdf

Météo-France. (2022b, October). *Monthly Climatological Bulletin, La Réunion, October 2022* (Tech. Rep.). 50, Bd du Chaudron, 97490 Ste-Clotilde, La Réunion: Direction Inter Régionale Océan Indien. Retrieved from https://donneespubliques.meteofrance.fr/donnees_libres/bulletins/BCMOM/BCMOM_974_202210.pdf

Michon, L., Di Muro, A., Villeneuve, N., Saint-Marc, C., Fadda, P., & Manta, F. (2013). Explosive activity of the summit cone of Piton de la Fournaise volcano (La Réunion island): a historical and geological review. *Journal of volcanology and geothermal research*, *264*, 117–133.

Morton, B. R., Taylor, G. I., & Turner, J. S. (1956). Turbulent gravitational convection from maintained and instantaneous sources. *Proceedings of the Royal Society of London. Series A. Mathematical and Physical Sciences*, *234*(1196), 1–23.

Moxnes, E. D., Kristiansen, N. I., Stohl, A., Clarisse, L., Durant, A., Weber, K., & Vogel, A. (2014). Separation of ash and sulfur dioxide during the 2011 Grímsvötn eruption. *Journal of Geophysical Research: Atmospheres*, *119*(12), 7477–7501.

Nadeau, P. A., Palma, J. L., & Waite, G. P. (2011). Linking volcanic tremor, degassing, and eruption dynamics via SO_2 imaging. *Geophysical research letters*, *38*(1).

National Academies of Sciences, Engineering, and Medicine. (2017). *Volcanic eruptions and their repose, unrest, precursors, and timing.* Washington, DC: The National Academies Press. doi: 10.17226/24650

Observatoire volcanologique du Piton de la Fournaise. (2022, January). *Monthly Bulletin, January 2022* (Tech. Rep. Nos. ISSN 2610 – 5101). 14RN3 Km 27, 97418 La Plaine des Cafres, La Réunion: Institut de physique du globe de Paris. Retrieved from https://www.ipgp.fr/volcanoweb/reunion/Bulletins-Communiques/2022/Bulletins/ovpf_20220201_bullmensu_en.pdf

Observatoire Volcanologique Du Piton De La Fournaise (OVPF), & Institut De Physique Du Globe De Paris (IPGP). (2008). *Seismic, tiltmeter, extensometer, magnetic and weather permanent networks on Piton de la Fournaise volcano and La Réunion [Dataset].* Institut de physique du globe de Paris (IPGP), Université de Paris. Retrieved from http://volobsis.ipgp.fr/networks/detail/PF doi: 10.18715/REUNION.PF

Oppenheimer, C., Scaillet, B., & Martin, R. S. (2011). Sulfur degassing from volcanoes:

source conditions, surveillance, plume chemistry and earth system impacts. *Reviews in Mineralogy and Geochemistry*, *73*(1), 363–421.

Overcamp, T. J. (1982). A statistical plume model with first-order decay. *Journal of Applied Meteorology (1962-1982)*, 1589–1593.

Pattantyus, A. K., Businger, S., & Howell, S. G. (2018). Review of sulfur dioxide to sulfate aerosol chemistry at Kīlauea Volcano, Hawai'i. *Atmospheric Environment*, *185*, 262–271.

Peltier, A., Bachèlery, P., & Staudacher, T. (2009). Magma transport and storage at Piton de La Fournaise (La Réunion) between 1972 and 2007: A review of geophysical and geochemical data. *Journal of Volcanology and Geothermal Research*, *184*(1-2), 93–108.

Prata, F., & Rose, B. (2015). Volcanic ash hazards to aviation. In *The encyclopedia of volcanoes* (pp. 911–934). Elsevier.

Pritchard, M., Poland, M., Reath, K., Andrews, B., Bagnardi, M., Biggs, J., ... Roman, A. (2022). *Optimizing satellite resources for the global assessment and mitigation of volcanic hazards – Suggestions from the USGS Powell Center Volcano Remote Sensing Working Group* (Tech. Rep.). US Geological Survey. (Scientific Investigations Report 2022–5116) doi: 10.3133/sir20225116

Queißer, M., Burton, M., Theys, N., Pardini, F., Salerno, G., Caltabiano, T., ... Kazahaya, R. (2019). TROPOMI enables high resolution SO_2 flux observations from Mt. Etna, Italy, and beyond. *Scientific reports*, *9*(1), 957.

Roult, G., Peltier, A., Taisne, B., Staudacher, T., Ferrazzini, V., Di Muro, A., & the OVPF team. (2012). A new comprehensive classification of the Piton de la Fournaise activity spanning the 1985–2010 period. Search and analysis of short-term precursors from a broad-band seismological station. *Journal of Volcanology and Geothermal Research*, *241*, 78–104.

Salerno, G., Burton, M., Oppenheimer, C., Caltabiano, T., Randazzo, D., Bruno, N., & Longo, V. (2009). Three-years of SO_2 flux measurements of Mt. Etna using an automated UV scanner array: Comparison with conventional traverses and uncertainties in flux retrieval. *Journal of Volcanology and Geothermal Research*, *183*(1-2), 76–83.

Seinfeld, J. H., & Pandis, S. N. (2016). *Atmospheric chemistry and physics: from air pollution to climate change*. John Wiley & sons.

Sellitto, P., Salerno, G., Corradini, S., Xueref-Remy, I., Riandet, A., Bellon, C., ... Legras, B. (2023). Volcanic Emissions, Plume Dispersion, and Downwind Radiative Impacts Following Mount Etna Series of Eruptions of February 21–26, 2021. *Journal of Geophysical Research: Atmospheres*, *128*(6), e2021JD035974. Retrieved from https://agupubs.onlinelibrary.wiley.com/doi/abs/10.1029/2021JD035974 (e2021JD035974 2021JD035974) doi: https://doi.org/10.1029/2021JD035974

Sen, A., & Srivastava, M. (2012). *Regression analysis: theory, methods, and applications*. Springer New York, NY. doi: 10.1007/978-1-4612-4470-7

Shreve, T., Grandin, R., & Boichu, M. (2022). Reservoir depressurization driven by passive gas emissions at Ambrym volcano. *Earth and Planetary Science Letters*, *584*, 117512.

Smittarello, D., Cayol, V., Pinel, V., Peltier, A., Froger, J.-L., & Ferrazzini, V. (2019). Magma propagation at Piton de la Fournaise from joint inversion of InSAR and GNSS. *Journal of Geophysical Research: Solid Earth*, *124*(2), 1361–1387.

Sparks, R. S. J., Bursik, M., Carey, S., Gilbert, J., Glaze, L., Sigurdsson, H., & Woods, A. (1997). *Volcanic plumes*. John Wiley & sons.

Stevens, J.-L. R., Rudiger, P., & Bednar, J. A. (2015). HoloViews: Building complex visualizations easily for reproducible science [Software]. In *Proceedings of the 14th python in science conference* (pp. 61–69).

Stewart, C., Damby, D. E., Horwell, C. J., Elias, T., Ilyinskaya, E., Tomašek, I., ... others (2022). Volcanic air pollution and human health: recent advances and future directions. *Bulletin of Volcanology*, *84*(1), 11.

Stohl, A., Prata, A., Eckhardt, S., Clarisse, L., Durant, A., Henne, S., ... others (2011). Determination of time-and height-resolved volcanic ash emissions and their use for quantitative ash dispersion modeling: the 2010 Eyjafjallajökull eruption. *Atmospheric Chemistry and Physics*, *11*(9), 4333–4351.

Surono, Jousset, P., Pallister, J., Boichu, M., Buongiorno, M. F., Budisantoso, A., ... Lavigne, F. (2012). The 2010 explosive eruption of Java's Merapi volcano–A '100-year' event. *Journal of Volcanology and Geothermal Research*, *241-242*, 121-135. Retrieved from https://www.sciencedirect.com/science/article/pii/S0377027312001862 doi: https://doi.org/10.1016/j.jvolgeores.2012.06.018

Tarantola, A. (2005). *Inverse problem theory and methods for model parameter*

estimation. SIAM.

Theys, N., Campion, R., Clarisse, L., Brenot, H., Van Gent, J., Dils, B., ... Ferrucci, F. (2013). Volcanic SO_2 fluxes derived from satellite data: a survey using OMI, GOME-2, IASI and MODIS. *Atmospheric Chemistry and Physics*, *13*(12), 5945–5968.

Theys, N., De Smedt, I., Lerot, C., Yu, H., & Van Roozendael, M. (2022). *S5P/TROPOMI SO_2 Algorithm Theoretical Basis Document (ATBD)* (Tech. Rep. No. S5P-BIRA-L2-400E-ATBD). Royal Belgian Institute for Space Aeronomy (BIRA-IASB), Brussels, Belgium: BIRA-IASB. (Tech. Rep. 2.4.1, BIRA, last accessed 2023-04-04, available at: https://sentinel.esa.int/documents/247904/2476257/Sentinel-5P-ATBD-SO2-TROPOMI)

Theys, N., De Smedt, I., Yu, H., Danckaert, T., van Gent, J., Hörmann, C., ... Van Roozendael, M. (2017). Sulfur dioxide retrievals from TROPOMI onboard Sentinel-5 Precursor: algorithm theoretical basis. *Atmospheric Measurement Techniques*, *10*(1), 119–153.

Theys, N., Fioletov, V., Li, C., De Smedt, I., Lerot, C., McLinden, C., ... others (2021). A sulfur dioxide Covariance-Based Retrieval Algorithm (COBRA): application to TROPOMI reveals new emission sources. *Atmospheric Chemistry and Physics Discussions*, *2021*, 1–42.

Theys, N., Hedelt, P., De Smedt, I., Lerot, C., Yu, H., Vlietinck, J., ... Van Roozendael, M. (2019). Global monitoring of volcanic SO_2 degassing with unprecedented resolution from TROPOMI onboard Sentinel-5 Precursor. *Scientific reports*, *9*(1), 2643.

Theys, N., Lerot, C., Brenot, H., Van Gent, J., De Smedt, I., Clarisse, L., ... Van Roozendael, M. (2022). Improved retrieval of SO_2 plume height from TROPOMI using an iterative Covariance-Based Retrieval Algorithm. *Atmospheric Measurement Techniques Discussions*, *2022*, 1–35.

Thomas, H. E., Watson, I. M., Carn, S. A., Prata, A. J., & Realmuto, V. J. (2011). A comparison of AIRS, MODIS and OMI sulphur dioxide retrievals in volcanic clouds. *Geomatics, Natural Hazards and Risk*, *2*(3), 217–232.

Tiesi, A., Villani, M., D'Isidoro, M., Prata, A., Maurizi, A., & Tampieri, F. (2006). Estimation of dispersion coefficient in the troposphere from satellite images of

volcanic plumes: Application to Mt. Etna, Italy. *Atmospheric Environment*, *40*(4), 628–638.

Tulet, P., & Villeneuve, N. (2011). Large scale modeling of the transport, chemical transformation and mass budget of the sulfur emitted during the April 2007 eruption of Piton de la Fournaise. *Atmospheric Chemistry and Physics*, *11*(9), 4533–4546.

Tupper, A., Textor, C., Herzog, M., Graf, H.-F., & Richards, M. S. (2009). Tall clouds from small eruptions: the sensitivity of eruption height and fine ash content to tropospheric instability. *Natural Hazards*, *51*, 375–401.

Veefkind, J. P., Aben, I., McMullan, K., Förster, H., De Vries, J., Otter, G., ... others (2012). TROPOMI on the ESA Sentinel-5 Precursor: A GMES mission for global observations of the atmospheric composition for climate, air quality and ozone layer applications. *Remote sensing of environment*, *120*, 70–83.

Verdurme, P., Carn, S., Harris, A. J., Coppola, D., Di Muro, A., Arellano, S., & Gurioli, L. (2022). Lava volume from remote sensing data: Comparisons with reverse petrological approaches for two types of effusive eruption. *Remote Sensing*, *14*(2), 323.

Vira, J., Carboni, E., Grainger, R. G., & Sofiev, M. (2017). Variational assimilation of IASI SO_2 plume height and total column retrievals in the 2010 eruption of Eyjafjallajökull using the SILAM v5.3 chemistry transport model. *Geoscientific Model Development*, *10*(5), 1985–2008.

Wagner, T., Warnach, S., Beirle, S., Bobrowski, N., Jost, A., Puķīte, J., & Theys, N. (2023). Investigation of three-dimensional radiative transfer effects for UV–Vis satellite and ground-based observations of volcanic plumes. *Atmospheric Measurement Techniques*, *16*(6), 1609–1662.

Williams, J. (1946). An approximation to the probability integral. *The Annals of Mathematical Statistics*, 363–365.